Thermal Science and Engineering Progress 69 (2026) 104416

Contents lists available at ScienceDirect

Thermal Science and Engineering Progress

journal homepage: www.elsevier.com/locate/tsep

Interplay of shear-dependent rheology and buoyancy forces in non-newtonian heat transfer

Razi Khan [a,b,*], Jorge Tiago [a], Adeel Ahmad [c], Paolo Valdiserri [d], Eugenia Rossi di Schio [d]

[a] Department of Mathematics and CEMAT, Instituto Superior Técnico, Universidade de Lisboa, Av. Rovisco Pais 1, Lisboa, 1049-001, Portugal
[b] Department of Mathematics and Physics, University of Campania Luigi Vanvitelli, Caserta, 81100, Italy
[c] Department of Mathematics, COMSATS University Islamabad, Park Road, Islamabad, 45550, Pakistan
[d] Department of Industrial Engineering, Alma Mater Studiorum - University of Bologna, viale Risorgimento 2, Bologna, 40136, Italy

ARTICLE INFO

Keywords:
Shear-dependent fluids
Reiner–philippoff model
Buoyancy-driven convection
Non-newtonian heat transfer
Semi-implicit scheme
Finite element approach

ABSTRACT

This study explore the fundamental mechanism governing buoyancy-driven flow and heat transfer of a shear-dependent non-Newtonian fluid modeled by Reiner–Philippoff (RPP) constitutive relation in an open-ended cavity with permeable horizontal surfaces. A finite element framework is implemented to solve the weak formulation of the coupled momentum and energy equations on a triangular mesh, using an implicit scheme for the linear terms and a semi-implicit approach for the transport terms. The study highlights the interplay between thermal gradients, shear-thinning and shear-thickening rheology, and buoyancy forces, demonstrating how non-Newtonian viscosity alterations influence convective transport, thermal boundary layers, and velocity profiles. The results reveal that higher Grashof numbers make upward flow motion much stronger and improve convective heat transmission. On the other hand, strong shear-rate dependencies cause localized changes in flow structure and thermal stratification. This study offers new insights into the physics of shear-dependent buoyancy-driven convection in open domains, contributing to a better understanding and modeling of non-Newtonian fluid systems which are important for engineering and industrial heat transfer applications including solar thermal receivers, electronic cooling, polymer extrusion, food processing, fire safety, and energy-efficient building designs.

1. Introduction

The last several decades have seen an exponential rise in the study of non-Newtonian fluid dynamics because of its widespread and frequent use in both natural and technological applications. It is more difficult to understand the engineering phenomena related to non-Newtonian fluids than it is to understand Newtonian fluids. Non-Newtonian fluids may exhibit viscoelastic, time-dependent, shear-thinning, and shear-thickening characteristics when suitable conditions are present. Among several empirical models [1–4], the RPP model [5,6] is one of the models that describes the non-Newtonian relationship between stress and strain. The RPP fluid model exhibits several behaviors, including pseudoplasticity (shear-thinning), dilatancy (shear-thickening), and Newtonian characteristics. Pseudoplastic fluids exhibit a decrease in viscosity as the shear rate increases. Yogurt, shaving cream, salad dressing, ketchup, and toothpaste are examples of pseudoplastic fluids. The phenomenon of ketchup that exhibits increased flow and decreases viscosity with increasing shear rate is a significant example. Dilatant fluids exhibit an increase in viscosity when exposed to shear force. The suspension of silica particles in polyethylene glycol, liquid armor, and a combination of cornflour and water are examples of dilatant fluids. These materials have a rheological behavior of increasing viscosity when subjected to shear stress. Given its extensive applications and duality in nature, the RPP model has received a lot of attention in the literature. Its interest covers many possible applications, mainly in medical and industrial fields [7,8]. A wide range of analyses have been conducted considering the flow phenomenon in the RRP model under different configurations.

Kapur and Gupta [9] examined the boundary layer flow of RPP fluids in a straight channel along its inlet length. They analyzed the two extreme cases in which the shear stress parameter is either minimal or maximal. Their research shows that changing three favorable factors can cause the viscosity coefficients to become more like those in the

* Corresponding author at: Department of Mathematics and CEMAT, Instituto Superior Técnico, Universidade de Lisboa, Av. Rovisco Pais 1, Lisboa, 1049-001, Portugal.
E-mail addresses: razi.khan@tecnico.ulisboa.pt, razi.khan@unicampania.it (R. Khan), jorge.tiago@tecnico.ulisboa.pt (J. Tiago), adeelahmed@comsats.edu.pk (A. Ahmad), paolo.valdiserri@unibo.it (P. Valdiserri), eugenia.rossidischio@unibo.it (E. Rossi di Schio).

https://doi.org/10.1016/j.tsep.2025.104416
Received 9 August 2025; Received in revised form 26 November 2025; Accepted 9 December 2025
Available online 10 December 2025

Newtonian model as the shearing rate gets closer to zero or infinity. Thus, this behavior makes the flow of such fluids more interesting. For shearing rate values that are moderate, the behavior is distinctly non-Newtonian, positioned between the two extremes of Newtonian behavior. The behavior is nearly Newtonian at shearing rate values that are either extremely low or exceedingly high. The study of how soluble matter moves in Newtonian flow through a circular tube presented by Taylor was expanded by Ghoshal [10] to non-Newtonian flows of Eyring and RPP model fluids. His investigation revealed that one could infer the Newtonian fluid from the relevant data of both types of fluids under study. In the study of Yam et al. [11] where they applied computational methods to systematically analyze the steady boundary layer flow of a RPP fluid, specifically focusing on the flow dynamics induced by a stretching wedge within a variable free stream. Their findings demonstrated that the unique solution is stable and that there are no multiple solutions as they analyzed the flow stability over a 90-degree wedge and through numerical simulations. Reddy et al. [12] further developed the RPP fluid flow across a stretched sheet and the thermal radiation effect. Their analysis suggests that with an increase in the Bingham number, there is a decrease in both the velocity and temperature profiles. Ishaq et al. [13] examined the magnetohydrodynamic flow of RPP fluid across a magnetized plate. Their study was primarily focused on conducting stability analysis to examine the impact of magnetic fields and fluid properties on flow stability. Ganesh et al. [14] investigated the heat transmission and melting flow of a RPP fluid across a surface, including a Darcy-Forchheimer medium. The analysis indicates that the velocity profile diminishes due to the Forchheimer and porosity variables, while the elevation of the temperature field corresponds to the temperature ratio parameter. The study by Kumar et al. [15] figured out how a RPP fluid would move across a vertical plate due to thermal radiation and a sinusoidal hydromagnetic effect. This study concentrated on qualitative and quantitative predictions of heat transfer in the gravity-induced regime. Arain et al. [16] examined the flow properties of two-dimensional RPP fluid in a moving channel where due to changes in viscosity, the fluid divided into two impermeable layers. The governing equations were simplified by employing the approximation of a low Reynolds number and long wavelength. We refer to publications [17–20] and the references provided for further reading on the subject.

Researchers have become more interested in the buoyancy-driven flows of viscous, incompressible fluids within cavities over the past few years, both numerically as well as experimentally [21]. This is mostly attributable to the diverse practical applications that arise from such flows. Applications of this nature encompass solar thermal receiver systems, electronic cooling, fire safety studies, and energy conservation in architecture. A critical aspect in these situations is the inherent geometry of buoyancy-driven flows and heat transfer within cavities, which significantly affects the interaction between the interior and exterior regions of the cavity, hence influencing flow and temperature distributions. Skok [22] conducted experimental and numerical investigations on a two-dimensional buoyancy-driven flow within a side-facing open cavity, with the objective of assessing flow patterns and quantifying both local and average Nusselt numbers for the cavity surfaces. Aydm [23] performed a numerical investigation to examine the transport processes of laminar coupled convection within a hollow influenced by shear and buoyancy forces. This work concentrated on the interplay between wall-induced forced convection and buoyancy-driven natural convection, offering enhanced understanding of the dynamics of these coupled phenomena. A comprehensive study was performed in [24] in order to determine the methodology for eliminating extended boundaries from open-ended structures in both two-dimensional and three-dimensional contexts. A comprehensive compilation of effective boundary conditions was obtained, incorporating a diverse array of regulating parameters for both temperature and flow fields. In their detailed study, Angirasa et al. [25] used numerical simulations to look at heat transport and transient as well as steady-state laminar buoyancy-driven flows within a square cavity with one open side. The findings of their study revealed that the boundary conditions on the open side exerted a little influence on natural convection within the cavity, principally affecting only a small area near the entrance with minimal implications for the broader computational domain. Following a very similar pattern, Stefanovic [26] numerically studied the unsteady flow of a thick, incompressible fluid inside a rectangular cavity. He looked at how the flow changed when shear forces and buoyancy effects came together. Polat et al. [27] further advanced the research by numerically examining laminar natural convection in inclined, open, shallow cavities. In this analysis, they were more concentrated on scenarios where the end-wall experienced constant heat flow and the walls that were not in contact with the heated surface experienced adiabatic conditions. This helped them to understand how the angle of the cavity affected the whole heat transfer process. The volumetric flow rate and heat transfer developed with a rise of aspect ratio and Rayleigh number, although heat transfer exhibits asymptotic behavior at a certain aspect ratio. Belgin [28] performed a numerical analysis of natural convection heat transport in differentially heated square cavities including horizontally oriented thin fins. This analysis used vertical isothermal walls and adiabatic horizontal walls creating the hollow, with a thin fin attached to the hot wall. Hossain et al. [29] investigated the unsteady natural convection flow of a viscous, incompressible fluid induced by differential heating along the solid vertical wall of an open-end rectangular cavity. This research was more concentrated on the investigation of the flow dynamics within a cavity containing two horizontal permeable surfaces, that are kept at the temperature of the ambient fluid. Their investigation yielded significant insights into the impact of temperature gradients along the walls of the cavity on fluid motion and heat transfer dynamics in systems with open and permeable boundaries. The study of Lefauve and Linden [30] examined buoyancy-driven flows in an inclined ducts. Their research was more focused on the investigation of the dynamics of constant stratified shear flows, focusing on three dependent variables: the qualitative flow regime, mass flux, and interfacial thickness. The research in [31] investigated the phenomenon of transient thermocapillary convection flows within a rectangular chamber including a uniformly heated side wall, conducted under zero-gravity settings. This study encompassed scaling analysis and numerical modeling. A simulation employing two-dimensional numerical techniques has been conducted. Shahabad et al. [32] studied the controlling strategy of the natural convection of a non-Newtonian fluid using a flexible fin analyzing the dilatant and pseudoplastic effects. Joshi [33] conducted a numerical investigation on the impact of aspect ratio on vorticity dynamics in a two-dimensional rectangular lid-driven cavity with a vertical temperature gradient and a compressible fluid. The research in [34] examined the mixed convection heat transfer of non-Newtonian fluid-structure interaction within an open trapezoidal cavity. They determined that for low Richardson numbers, shear-thickening fluids show higher Nusselt numbers, whereas at high Richardson numbers, shear-thinning fluids demonstrate higher values. For more studies on the topic we refer the articles [35–38] and the references cited therein.

1.1. Research aims and novel contributions

- To analyze buoyancy-driven flow in conjunction with non-Newtonian fluid dynamics using the RPP model (rate-type) in an open-end rectangular cavity.
- Utilize the finite element method with semi-implicit time-stepping scheme for computational analysis.
- Investigate the intricate relationships between heat transfer and non-Newtonian fluid dynamics under different flow configuration.
- To offer a solid mathematical framework for theoretical study of non-Newtonian fluids.

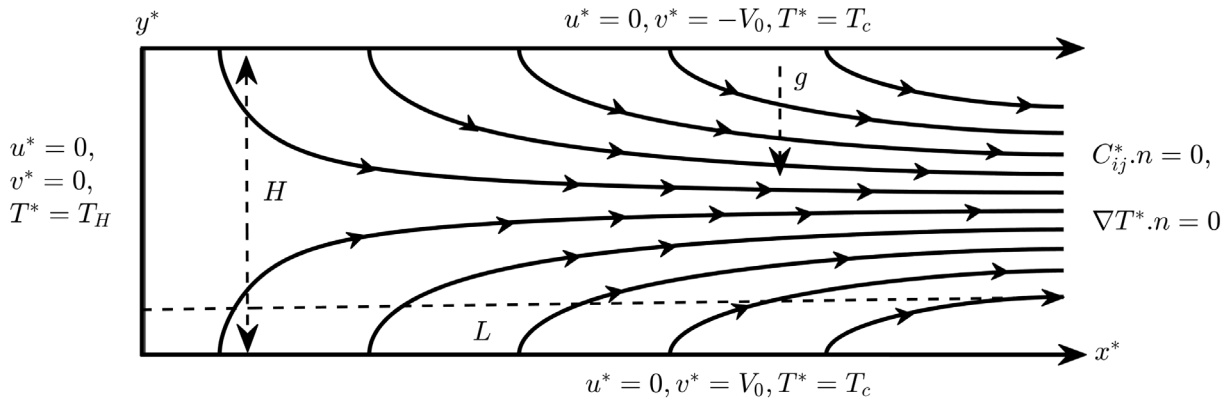

Fig. 1. Geometrical interpretation.

- To elucidate the implications of non-Newtonian fluid behavior for diverse industrial applications where controlling fluid flow and heat transmission is essential.
- Applications of RPP model in an open-ended cavity with a combined finite element method and semi-implicit scheme to study the buoyancy-driven flow and heat transfer, which has received less attention in literature.

2. Mathematical formulation

The aim of this section is to model the unsteady two-dimensional flow of a viscous, incompressible, non-Newtonian RPP fluid within an open-ended cavity. The cavity's vertical wall is maintained at a constant temperature, T_H, while the horizontal surfaces are at the ambient fluid temperature, T_c. We assume that the horizontal surfaces are permeable, facilitating consistent fluid transpiration across both the upper and lower surfaces. Fig. 1 illustrates the geometric characteristics and flow configuration. The governing equations that characterize the problem, concerning the fluid dynamics, can be represented as follows:

$$\nabla \cdot \overset{*}{\mathbf{u}} = 0 \tag{1}$$

$$\rho \frac{D\overset{*}{\mathbf{u}}}{D\overset{*}{t}} = \nabla \cdot \overset{*}{\mathbf{C}} + \boldsymbol{g}\beta_T(\overset{*}{T} - T_c) \tag{2}$$

In this context, the velocity components in the $\overset{*}{x}$ and $\overset{*}{y}$ directions are denoted by $\overset{*}{\mathbf{u}} = (\overset{*}{u}, \overset{*}{v})$. The material time derivative is represented by $\frac{D}{D\overset{*}{t}}$. The symbol ρ signifies density, $\boldsymbol{g}$ denotes gravitational acceleration vector, β_T represents the temperature volumetric expansion coefficient, $\overset{*}{T}$ indicates temperature, and the Cauchy stress tensor $\overset{*}{\mathbf{C}}$ is expressed as follows:

$$\overset{*}{\mathbf{C}} = -\overset{*}{p}I + \overset{*}{\tau}. \tag{3}$$

where I denotes the identity and $\overset{*}{\tau}$ signifies the deviatoric stress tensor

$$\overset{*}{\tau} = \begin{pmatrix} \overset{*}{\tau}_{xx} & \overset{*}{\tau}_{xy} \\ \overset{*}{\tau}_{yx} & \overset{*}{\tau}_{yy} \end{pmatrix} \tag{4}$$

The rheological relation between the deviatoric stress $\overset{*}{\tau}$ and the strain-rate tensor

$$\overset{*}{e}(\overset{*}{\mathbf{u}}) = \frac{\nabla\overset{*}{\mathbf{u}} + (\nabla\overset{*}{\mathbf{u}})^T}{2} \tag{5}$$

is given by the following expression:

$$\overset{*}{\tau} = \left[\mu_\infty + \frac{\mu_0 - \mu_\infty}{1 + \frac{\overset{*}{\tau}^2}{2\overset{*}{\tau_0}^2}}\right]\overset{*}{e}, \tag{6}$$

where μ_0 and μ_∞ represent the zero shear and upper Newtonian limiting viscosities, respectively, $\overset{*}{\tau_0}$ is the reference shear stress. We remark that $\overset{*}{\tau_0}^2$, $\overset{*}{\tau}^2$ are the respective tensor contractions, operation which, for a general bi-dimensional tensor τ, is given by $\tau^2 = \tau : \tau = \sum_{k=1}^{2}\sum_{l=1}^{2}\tau_{kl}\tau_{lk}$. As to the temperature, its distribution is given by the equation:

$$\frac{D\overset{*}{T}}{D\overset{*}{t}} = \alpha\nabla^2\overset{*}{T} \tag{7}$$

Let Ω to represent the cavity domain represented in Fig. 1. We denote the boundary of Ω by $\partial\Omega = \Gamma_L \cup \Gamma_B \cup \Gamma_U \cup \Gamma_R$, which is composed by the left vertical wall (Γ_L), the bottom permeable wall (Γ_B), the upper permeable wall (Γ_U), and the right open-end (Γ_R), respectively. The coupled system of Eqs. (1)–(7) is supplemented with the boundary conditions:

$$\begin{cases} \overset{*}{u} = \overset{*}{v} = 0, \overset{*}{T} = T_H & \text{on } \Gamma_L \\ \overset{*}{u} = 0, \overset{*}{v} = V_0, \overset{*}{T} = T_c & \text{on } \Gamma_B \\ \overset{*}{\mathbf{C}} \cdot n = 0, \nabla\overset{*}{T} \cdot n = 0 & \text{on } \Gamma_R \\ \overset{*}{u} = 0, \overset{*}{v} = -V_0, \overset{*}{T} = T_c & \text{on } \Gamma_U \end{cases} \tag{8}$$

and initial conditions

$$\overset{*}{u} = 0, \overset{*}{v} = 0, \overset{*}{T} = 0 \quad \text{at } \overset{*}{t} = 0.$$

For the purpose of non-dimensionalization of the equations, we introduce the following new variables as a linear combination of the original variables:

$$\begin{cases} u = \frac{\overset{*}{u}}{V_0}, v = \frac{\overset{*}{v}}{V_0}, x = \frac{\overset{*}{x}}{H}, y = \frac{\overset{*}{y}}{H}, t = \frac{V_0\overset{*}{t}}{H}, \\ T = \frac{\overset{*}{T}-T_c}{T_H-T_c}, p = \frac{\overset{*}{p}}{\rho V_0^2}, \tau = \frac{H\overset{*}{\tau}}{V_0\mu_\infty}, \tau_0 = \frac{H\overset{*}{\tau_0}}{V_0\mu_\infty}. \end{cases} \tag{9}$$

as well as the dimensionless parameters

$$\begin{cases} Re = \frac{\rho V_0 H}{\mu_\infty}, \quad Pr = \frac{\mu_\infty}{\rho\alpha}, \\ Ra = \frac{g\beta_T\rho(T_H-T_c)H^3}{\mu_\infty\alpha}, \quad Gr = \frac{Ra}{Pr}. \end{cases} \tag{10}$$

In this context, Re denotes the Reynolds number, representing the ratio of inertial forces to viscous forces, whereas Pr, the Prandtl number, reflects the relative influence of momentum diffusivity to heat diffusivity. The Rayleigh number Ra characterizes buoyancy-driven flow by balancing thermal expansion forces with viscous forces. The Grashof number Gr, defined as the ratio of Ra to Pr, indicates the impact of buoyant forces in comparison to momentum diffusivity, emphasizing the intensity of natural convection. Collectively, these

parameters establish a thorough framework for examining the interplay between fluid dynamics and thermal transfer processes.

Using these dimensionless variables and parameters, the governing system of equations reduces to:

$$\frac{\partial u}{\partial x}+\frac{\partial v}{\partial y}=0, \tag{11}$$

$$\frac{\partial u}{\partial t}+u\frac{\partial u}{\partial x}+v\frac{\partial u}{\partial y}=-\frac{\partial p}{\partial x}+\frac{1}{Re}\left(\frac{\partial \tau_{xx}}{\partial x}+\frac{\partial \tau_{xy}}{\partial y}\right) \tag{12}$$

$$\frac{\partial v}{\partial t}+u\frac{\partial v}{\partial x}+v\frac{\partial v}{\partial y}=-\frac{\partial p}{\partial y}+\frac{1}{Re}\left(\frac{\partial \tau_{yx}}{\partial x}+\frac{\partial \tau_{yy}}{\partial y}\right)+\frac{Gr}{Re^2}T \tag{13}$$

$$\frac{\partial T}{\partial t}+u\frac{\partial T}{\partial x}+v\frac{\partial T}{\partial y}=\frac{1}{PrRe}\left(\frac{\partial^2 T}{\partial x^2}+\frac{\partial^2 T}{\partial y^2}\right) \tag{14}$$

Finally, the dimensionless boundary conditions, associated with the system (11)–(14) are:

$$\begin{cases} u=0, v=0, T=1, & \text{at} \quad x=0 \\ \mathbf{C}\cdot n=0, \nabla T\cdot n=0, & \text{at} \quad x=A \\ u=0, v=s, T=0, & \text{at} \quad y=0 \\ u=0, v=-s, T=0, & \text{at} \quad y=1 \end{cases} \tag{15}$$

where $A=\frac{L}{H}$ is the length of the cavity and s represents the suction/blowing parameter.

Let us now remark that, from (4) and (9) we have:

$$\tau^2=\sum_{k=1}^{2}\sum_{l=1}^{2}\tau_{kl}\tau_{lk}=\tau_{xx}^2+2\tau_{xy}^2+\tau_{yy}^2, \tag{16}$$

where we used the symmetry of the stress: $\tau_{xy}=\tau_{yx}$. Similarly, from (5), we see that $e(u)$ is given by

$$e_{xx}=\frac{\partial u}{\partial x}, e_{yy}=\frac{\partial v}{\partial y}, e_{xy}=\frac{1}{2}\left(\frac{\partial u}{\partial y}+\frac{\partial v}{\partial x}\right). \tag{17}$$

Therefore, using Eq. (6), we obtain the dimensionless form of the components of the stress:

$$\tau_{xx}=\left[1+\frac{\lambda-1}{1+\left(\frac{1}{2\tau_0^2}\right)\left(\tau_{xx}^2+2\tau_{xy}^2+\tau_{yy}^2\right)}\right]\frac{\partial u}{\partial x} \tag{18}$$

$$\tau_{yy}=\left[1+\frac{\lambda-1}{1+\left(\frac{1}{2\tau_0^2}\right)\left(\tau_{xx}^2+2\tau_{xy}^2+\tau_{yy}^2\right)}\right]\frac{\partial v}{\partial y} \tag{19}$$

$$\tau_{xy}=\frac{1}{2}\left[1+\frac{\lambda-1}{1+\left(\frac{1}{2\tau_0^2}\right)\left(\tau_{xx}^2+2\tau_{xy}^2+\tau_{yy}^2\right)}\right]\left(\frac{\partial u}{\partial y}+\frac{\partial v}{\partial x}\right), \tag{20}$$

We are also interested in capturing the Newtonian and non-Newtonian behaviors of the model and, for this purpose, we consider $\tau=\mu(\tau^2)e(u)$ with the viscosity parametrized by

$$\mu(\tau^2)=\left[1+\frac{\lambda-1}{1+\left(\frac{\tau^2}{2\beta^2}\right)}\right] \tag{21}$$

where

$$\beta=\sqrt{\tau_0^2}, \quad \beta>0.$$

Having $\mu(.)$ parametrized by λ and β will allow us to easily distinguish between Newtonian (for instance for $\lambda=1$, or for both very small or very large values of β) and different non-Newtonian rheologies such as shear-thinning, for $\lambda>1$, and shear-thickening, for $\lambda<1$.

Fig. 2 illustrates the RPP model's correlation between apparent viscosity and shear stress as a function of shear rate. The results show substantial shear-thinning behavior, with viscosity decreasing as shear rate increases. This behavior is consistent with experimental observed trends for a wide range of non-Newtonian fluids, including polymer melts, blood, and biofluids. As the shear rate increases, the model exhibits a strong shear-thickening response, showing an increase in apparent viscosity proportional to the deformation rate, similar to the behavior of concentrated suspensions and certain polymeric solutions. The model predicts a quasi-Newtonian plateau at low shear rates, while the viscosity asymptotically approaches a constant value at high shear rates, reflecting a physically anticipated transition as demonstrated by rheometric measurements. These characteristics indicate that the RPP model accurately depicts the shear-dependent features and nonlinear rheological response that are frequently observed in experimental investigations [39–41].

For a better understanding of the fluid velocity behavior of the fluid we will also consider and analyze the well known stream-function ψ, which adheres to the Poisson equation:

$$\nabla^2\psi+\omega=0,$$

where ∇^2 represents the Laplacian operator, and the term ω in this equation is the vorticity, which is defined as:

$$\omega=\frac{\partial v}{\partial x}-\frac{\partial u}{\partial y}.$$

The velocity components u and v are associated with the stream function ψ through:

$$u=\frac{\partial \psi}{\partial y} \quad \text{and} \quad v=-\frac{\partial \psi}{\partial x}.$$

3. Numerical approach and code validation

To find the solution of the model described by the coupled nonlinear system of PDE's (11)–(14) we need to rely on numerical methods. Here, we adopt an implicit time discretization with a semi-implicit treatment of the convective terms in Eqs. (12)–(14). In this analysis, we consider the time interval $I_t=(0,t_f)$ and partition it into discrete sub-intervals, or time steps, represented by $I^m=(t^m,t^{m+1})$ for $m=0,1,\ldots,N$. Each sub-interval has a constant duration as specified by $t^{m+1}-t^m=\Delta t$. This technique divides the space-time domain $I_t\times\Omega$ into several time slabs $I^m\times\Omega$. For each time slab, we assume that the solution at $t=t^m$ is known, allowing us to compute the solution at the next time $t=t^{m+1}$. This assumption holds true because the approximate solution at $t=0$ is established based on the initial data. We are then left with a sequence of space-dependent problems to solve.

To discretize in space, we will consider approximated solutions of the corresponding weak formulation, searched in certain finite element spaces, which we will briefly describe in the following. Consider $\Omega\subset\mathbb{R}^2$ to be a bounded two-dimensional domain which can be exactly described with a triangulation, denoted by Ω_κ, which divides Ω into smaller, non-overlapping triangles. Mathematically, the triangulation Ω_κ is a collection of triangles K such that:

$$\bigcup_{K\in\Omega_\kappa}K=\Omega\,.$$

This means that the union of all triangles K in the triangulation Ω_κ exactly covers the entire domain Ω. Additionally, it is essential that any two triangles in the triangulation do not overlap. Formally, for any two distinct triangles K_i and K_j in Ω_κ:

$$K_i\cap K_j=\emptyset \quad \text{for} \quad i\neq j\,.$$

This ensures that the intersection of any two different triangles is empty, meaning that they share no common interior points. In addition, Ω_κ must be a regular triangulation, in the sense that each triangle should not be too stretched (see [42] for more details). We are now in conditions to define the finite element spaces.

$$V_h=\left\{\mathbf{u}\in H^1(\Omega)\cap C(\bar{\Omega})\mid \forall\, K\in\Omega_\kappa, \mathbf{u}\mid_K\in P_2\right\} \tag{22}$$

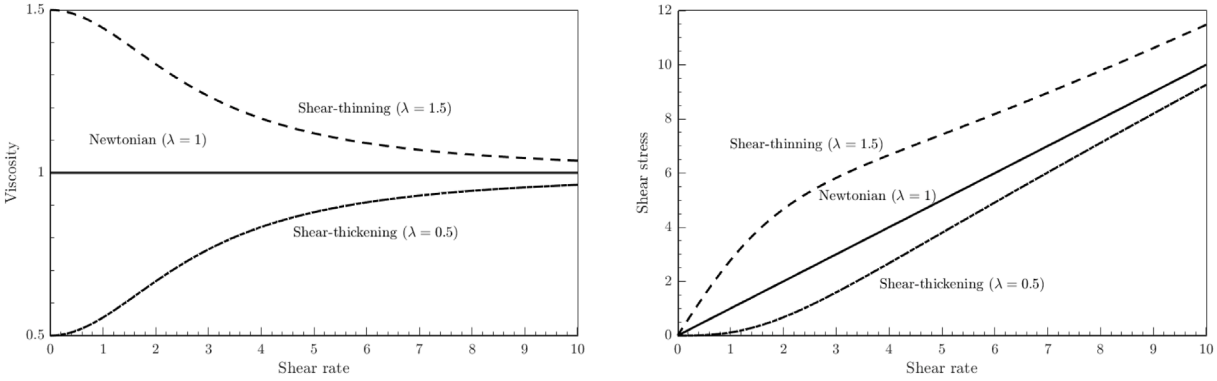

Fig. 2. Rheological behavior of the RPP model showing the dependence of apparent viscosity (left) and shear stress (right) on shear rate.

$$Q_h = \left\{ p \in L^2(\Omega) \mid \forall\, K \in \Omega_\kappa,\ p\,|_K \in P_1 \right\} \tag{23}$$

and $\mathbf{V}_h = V_h \times V_h$ where the Sobolev space $H^1(\Omega)$ is defined as:

$$H^1(\Omega) = \left\{ u \in L^2(\Omega) \mid \frac{\partial u}{\partial x_i} \in L^2(\Omega) \text{ for } i = 1, 2 \right\}, \tag{24}$$

and P_1 and P_2 are the spaces of polynomials of degrees 1 and 2, respectively. Additionally, we define the subspace

$$V_{h,0} = \left\{ \mathbf{u} \in V_h \mid \mathbf{u} = 0 \text{ on } \Gamma_L \cup \Gamma_B \cup \Gamma_U \right\} \tag{25}$$

and $\mathbf{V}_{h,0} = V_{h,0} \times V_{h,0}$.

Then, for each $k \in 0, 1, \ldots, N$, assuming $(\mathbf{u}^k, p^k, T^k)$ known, we look for $(\mathbf{u}^{k+1}, p^{k+1}, T^{k+1}) \in \mathbf{V}_h \times Q_h \times V_h$ solution of the following approximated weak formulation of system (11)–(14):

$$\int_\Omega \left[\frac{\mathbf{u}^{k+1} - \mathbf{u}^k}{\Delta t} \cdot \overline{v} + (\mathbf{u}^k \cdot \nabla)\mathbf{u}^{k+1} \cdot \overline{v} + \frac{1}{Re}\left[\mu\left(e^2(\mathbf{u}^k)\right) e(\mathbf{u}^{k+1}) : \nabla \overline{v} - p(\nabla \cdot \overline{v}) \right] - \frac{Gr}{Re^2} T^{k+1} \overline{v} \right] dx = 0, \quad \forall \overline{v} \in \mathbf{V}_{h,0} \tag{26}$$

$$\int_\Omega \left[\frac{T^{k+1} - T^k}{\Delta t} \bar{\phi} + (\mathbf{u}^k \cdot \nabla) T^{k+1} \bar{\phi} + \frac{1}{PrRe} \left(\nabla T^{k+1} \cdot \nabla \bar{\phi} \right) \right] dx = 0, \quad \forall \bar{\phi} \in V_{h,0} \tag{27}$$

$$\int_\Omega (\nabla \cdot \mathbf{u}^{k+1}) \bar{q}\, dx = 0, \quad \forall \bar{q} \in Q_h \tag{28}$$

with boundary conditions

$$\begin{cases} u^{k+1} = v^{k+1} = 0,\ T^{k+1} = 1 & \text{on } \Gamma_L \\ u^{k+1} = 0,\ v^{k+1} = V_0,\ T^{k+1} = 0 & \text{on } \Gamma_B \\ u^{k+1} = 0,\ v^{k+1} = -V_0,\ T^{k+1} = 0 & \text{on } \Gamma_U \end{cases} . \tag{29}$$

We remark that, for simplicity, we have discretized $\tau = \mu(\tau^2)e(u)$ explicitly as $\mu\left(e^2(\mathbf{u}^k)\right) e(\mathbf{u}^{k+1})$.

Since V_h, $\mathbf{V}_h$ and Q_h are finite dimensional spaces, it turns out that solving the system (26)–(29) is equivalent to solve a finite dimensional linear system with large dimension. We refer to [43] for more details about the finite element discretization of coupled systems of PDE's.

To implement the solution of (26)–(29) FreeFEM++ [44] was used. To test the implementation we performed an analysis of the convergence of the solution with respect to mesh refinement. Since we do not have an exact to solution, we considered, as a reference solution, the solution obtained on a fine mesh with 193 × 65 vertices, which corresponds to 49665 degrees of freedom (DOFs) for P_2 approximations (velocity and temperature) and to 12545 DOFs for a P_1 approximation (pressure).

Once we obtain the reference solution, we then compute the same variables on a coarser mesh using reduced degrees of freedom. The objective is to quantify the relative errors for each variable between the coarse and fine mesh solutions. To determine the global error magnitude for each variable, these relative errors are calculated using the L^2 norm. For instance, the relative error between the first component of the velocity u obtained for a coarse mesh and the reference one is given by:

$$\text{Relative Error} = \frac{\|u_{\text{fine}} - u_{\text{coarse}}\|_{L^2}}{\|u_{\text{fine}}\|_{L^2}}$$

where $\|u\|_{L^2}$ is the L^2-norm. Similarly, we obtained the relative errors for the variables v, ψ, p and T.

Table 1
Relative Errors against P_2 and P_1 Degrees of Freedom.

P_2 DOFs/P_1 DOFs	Relative Errors				
	$u(P_2)$	$v(P_2)$	$\psi(P_1)$	$p(P_1)$	$T(P_2)$
133/40	0.14738	1.57872	0.11794	0.18944	2.08239
363/102	0.01397	0.12414	0.05850	0.02137	0.23001
2133/560	0.00285	0.01381	0.00712	0.00994	0.05232
6721/1728	0.00139	0.00660	0.00219	0.00798	0.02282
11907/3040	0.00109	0.00550	0.00116	0.00683	0.01482
21505/5461	0.00081	0.00427	0.00062	0.00566	0.00738

The results obtained at $t = 3$ are shown in Table 1. Convergence is observed for all the variables under analysis.

For numerical computations, we employ a mesh of 193 × 65 vertices as illustrated in Fig. 3, with a time step of 0.01 and continuing until reached steady state. This choice is supported by the fact that there is sufficient precision when the variations in values at different mesh points become insignificant. We further tested the implementation using mesh refinement tests at various time steps, verifying the results' convergence and consistency. To verify the accuracy of the employed numerical method, simulations of the classical two-dimensional lid-driven cavity flow were conducted for Reynolds number $Re = 1000$. This benchmark problem uses as a standard test for validating incompressible Navier–Stokes solvers, given the availability of high-accuracy reference solutions. The horizontal and vertical velocity profiles calculated along the cavity centerlines (Fig. 4) were compared with benchmark data from Ghia et al. [45], Mustafa [46], and other established results [47,48]. The strong alignment between the current findings and the reference data validates the robustness and reliability of the numerical scheme employed.

To further reinforce the validity of the present numerical implementation, the solver was subsequently applied to the mixed convection (buoyancy-assisted) lid-driven cavity problem. While Fig. 4 already demonstrates strong agreement between the present velocity profiles and the benchmark data of Ghia et al. [45] for the classical lid-driven cavity at Re = 1000, the additional comparisons in Tables 2 and 3 extend this verification to thermally driven flows. Specifically, the computed extrema of the horizontal and vertical velocity components

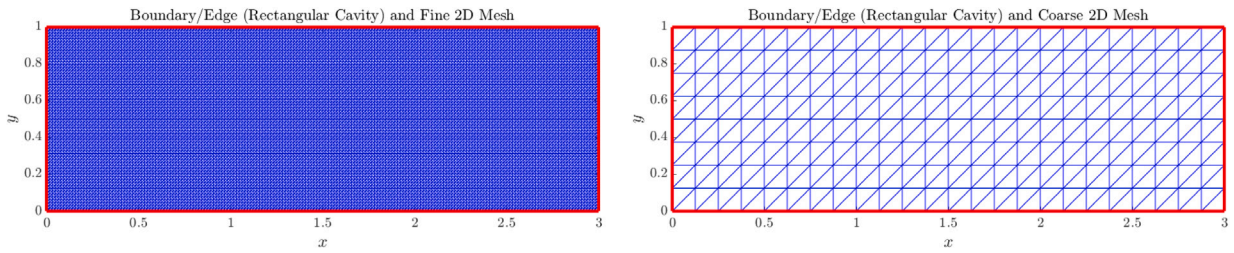

Fig. 3. The fine mesh contains 24 576 triangular elements and 12 545 vertices, while the coarse mesh consists of 384 triangular elements and 225 vertices.

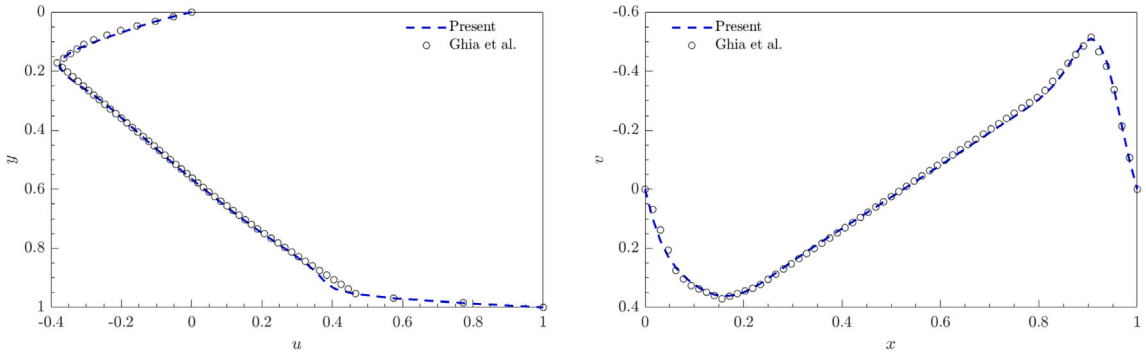

Fig. 4. Comparison of velocity profiles between the present study and the benchmark results of Ghia et al. [45]: (**left**) Horizontal velocity (u) along the vertical centerline at Re = 1000; (**right**) Vertical velocity (v) along the horizontal centerline at Re = 1000.

Table 2
Comparison of the computed minimum and maximum horizontal and vertical velocities in the lid-driven cavity with published results for $Gr = 100$, and $\lambda = 1$.

	Present results	Waheed [49]	Abdelkhaleq [50]	Khanafer & Chamkha [51]	Iwatsu et al. [52]
$Re = 100$					
u_{min}	−0.212478	−0.21198	−0.2147	−0.2122	−0.2037
u_{max}	1.00000	1.00000	1.0000	1.0000	1.0000
v_{min}	−0.248271	−0.251027	−0.2485	−0.2506	−0.2448
v_{max}	0.176100	0.177125	0.1703	0.1765	0.1699

Table 3
Comparison of the computed minimum and maximum horizontal and vertical velocities in the lid-driven cavity with published results for $Gr = 100$, and $\lambda = 1$.

	Present results	Waheed [49]	Abdelkhaleq [50]	Khanafer & Chamkha [51]	Iwatsu et al. [52]
$Re = 400$					
u_{min}	−0.325838	−0.31871	−0.3104	−0.3099	−0.3179
u_{max}	1.00000	1.00000	1.0000	1.0000	1.0000
v_{min}	−0.448576	−0.441064	−0.4435	−0.4363	−0.4459
v_{max}	0.299972	0.294505	0.2903	0.2866	0.2955

at $Re = 100$ and $Re = 400$ exhibit excellent agreement with the established results reported by Waheed [49], Abdelkhaleq [50], Khanafer and Chamkha [51], and Iwatsu et al. [52]. This close correspondence confirms the solver's robustness and accuracy not only for purely forced convection but also for buoyancy-influenced mixed convection regimes. The consistency of these results across both benchmark problems validates the reliability of the adopted numerical approach for simulating incompressible non-Newtonian and thermally driven flows.

3.1. Validation against benchmark power-law model

To validate the proposed RPP formulation for non-Newtonian behavior, we compared our results with benchmark lid-driven cavity studies for generalized Newtonian (power-law) fluids available in the literature. In particular, the velocity distributions along the horizontal and vertical centerlines were compared with those reported by Neofytou [53] and Bell et al. [54].

Although the constitutive laws differ (RPP versus power-law), both models exhibit comparable rheological characteristics under shear: for $\lambda > 1$, the RPP fluid displays shear-thinning behavior similar to a power-law fluid with $n < 1$, while $\lambda < 1$ corresponds to shear-thickening behavior analogous to $n > 1$.

Fig. 5 presents the velocity components $u(y)$ (left) and $v(x)$ (right) along the vertical and horizontal centerlines, respectively. The RPP results reproduce the same qualitative and quantitative trends as those in the benchmark power-law studies capturing the expected variations in velocity magnitude and flow structure. This agreement confirms the physical consistency and reliability of the present numerical formulation for non-Newtonian flow regimes.

4. Results and discussion

This section initially focuses on the viscosity characteristics of the model prior to its integration into the complete coupled system. Doing

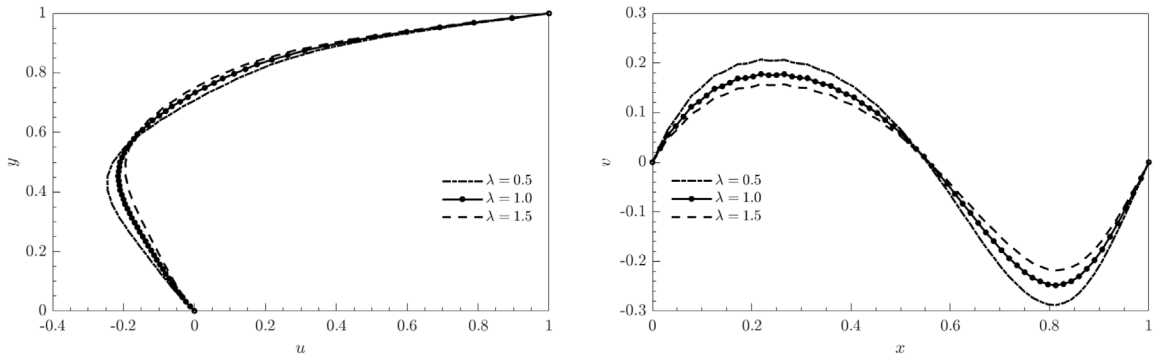

Fig. 5. Validation of the RPP model against power-law benchmarks: centerline velocity profiles showing consistent shear-thinning ($\lambda > 1$) and shear-thickening ($\lambda < 1$) behavior.

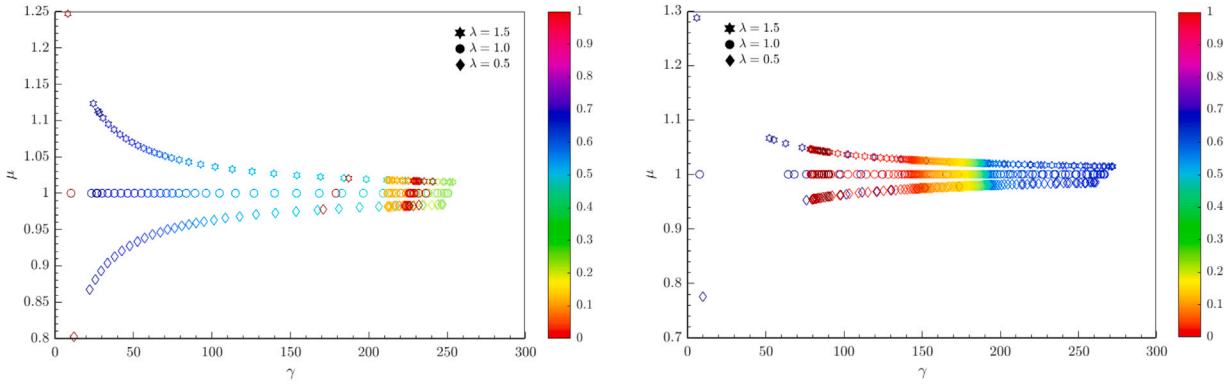

Fig. 6. Dependence of the viscosity μ on the shear rate γ for various values of the shear-thinning and shear-thickening parameter λ. The plot on the left corresponds to $x = 0.5$, the plot on the right corresponds to $y = 0.5$.

so will enable us to thoroughly examine the impact of viscosity behavior and its influence on the model's dynamics prior to coupling the system. Secondly, we study the model's Newtonian response at low and high reference shear stresses, providing a thorough understanding of its behavior in a range of flow conditions. We then couple the system and investigate the impact of buoyancy and thermal effects on temperature, velocity, and viscosity profiles. Finally, we concentrate on the behavior of the local and average Nusselt numbers, which reveal details about the system's overall heat transport characteristics.

4.1. Viscosity based analysis

We start by presenting the results for the solution of (11)–(13) without considering the coupling with the temperature variable. Fig. 6 illustrates the spatial variation in viscosity μ as a function of shear rate γ along the cavity centerlines $x = 0.5$ and $y = 0.5$ for different RPP parameter values λ, demonstrating shear-thinning ($\lambda = 1.5$), Newtonian ($\lambda = 1$), and shear-thickening ($\lambda = 0.5$) tendencies. These plots illustrate that an increase in shear rate results in decreased viscosities for shear-thinning fluids and increased viscosities for shear-thickening fluids, consistent with the expected rheological behavior shown in Fig. 2.

To better analyze the rheological behavior of the RPP model at both the bottom and top walls, we define the mean skin friction coefficient as a measure of the average nondimensional wall shear stress along the wall surface. The local skin friction coefficient is given by

$$c_f(x) = \frac{2\,\tau_{xy}}{V_0^2} = \frac{2\mu(\tau^2)}{Re}\left(\frac{\partial u}{\partial y} + \frac{\partial v}{\partial x}\right)_{y=y_0,y_1}, \tag{30}$$

where $y = y_0, y_1$ corresponds to bottom and top walls respectively. The mean skin friction coefficient is then defined as the spatial average of $c_f(x)$ along the wall segment $[x_0 = 0, x_1 = 3]$:

$$c_F = \frac{1}{x_1 - x_0}\int_{x_0}^{x_1} c_f(x)\,dx. \tag{31}$$

As depicted in Fig. 7, the variation of the skin friction coefficient clearly reflects the influence of non-Newtonian rheology governed by the RPP model. The fluid exhibits shear-thinning behavior, which reduces the local viscosity near the wall and consequently enhances the velocity gradient. This effect results in higher wall shear stress and, therefore, a larger magnitude of the skin friction coefficient. In contrast, for shear-thickening fluids, the viscosity increases under shear, making the flow near the wall less steep, which in turn reduces the skin-friction coefficient. The observed trend $|c_F|_{\lambda>1} > |c_F|_{\lambda=1} > |c_F|_{\lambda<1}$ is thus physically consistent with the expected rheological characteristics of the RPP model.

In Fig. 8, we show the velocity and viscosity profiles obtained under the shear-thickening (or dilatant), the shear-thinning (or pseudoplastic) and the Newtonian assumptions. These assumptions were modeled by choosing $\lambda < 1$, $\lambda > 1$ and $\lambda = 1$, respectively. Here it is essential to note that $U = \sqrt{u^2 + v^2}$ represents the magnitude of the velocity vector.

On the first two rows of Fig. 8, we depict the effect of suction ($s = 1$) through the permeable walls both for the shear-thickening regime (left column, $\lambda = 0.05$) and for the shear-thinning regime (right column, $\lambda = 5$). The shear-thickening behavior refers to a non-Newtonian fluid response where the viscosity of the fluid increases as the rate of shear within the rectangular cavity increases. As we can see in the viscosity representation, the increase of this quantity is more pronounced near the walls of the cavity due to the velocity gradient, causing the fluid to resist flow more in these regions compared to the center of the cavity. From the analysis of thinning behavior in the rectangular cavity as shown in Fig. 8 (second column), it is observed that the viscosity of the fluid is minimum (the red color representation) where the velocity

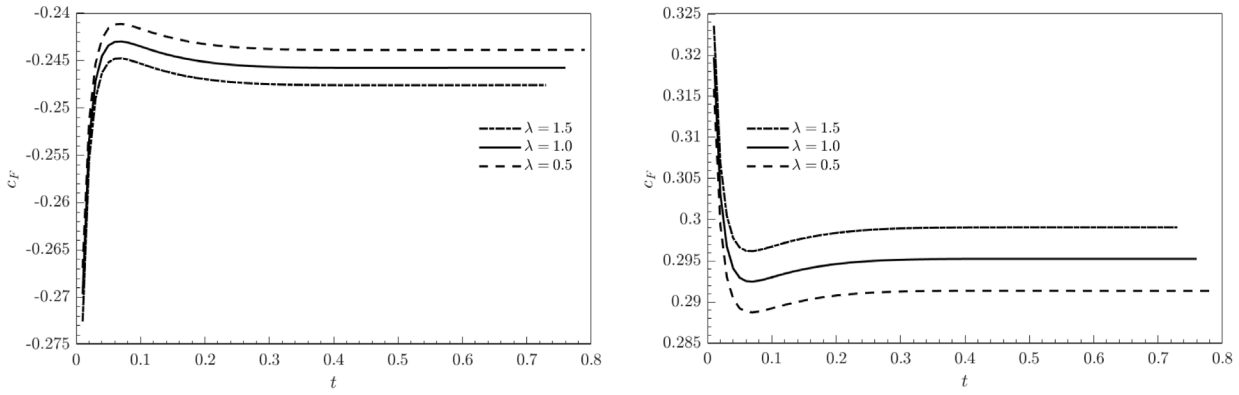

Fig. 7. Mean skin friction coefficient (c_F) at the top (left) and bottom (right) walls.

gradient is steeper (right half of the domain) due to the shear-thinning nature of the fluid.

On third and fourth rows of Fig. 8, we depicted the results for the blowing scenario ($s = -1$). As we can see for the case of shear-thickening, again the increased viscosity is comparatively more pronounced near the upper and bottom walls of the cavity than at the center of the cavity. We can see that the velocity magnitude tend to be higher near the walls, when compared to the case when $s = 1$, especially closer to the open-end wall. Globally, the viscosity has lower values for the blowing case. On the other hand, for the shear-thinning scenario (right column) it is observed that the viscosity is lower (the red color representation) where the velocity gradient is steeper due to the shear-thinning nature of the fluid. Besides, the viscosity is globally higher, for the blowing configuration, when compared to the suction case ($s = 1$).

In the last two rows of Fig. 8, we represent the results for $\lambda = 1$, for $s = -1$, on the left and $s = 1$, on the right. The velocity of the fluid at the horizontal surfaces is maximum and least near the middle of the cavity ($y = 0.5$), depending on the porous surfaces. Furthermore, it should be noted that the fluid's velocity increases as it moves from the left wall ($x = 0$) to the right open-end wall ($x = 3$) of the cavity due to the push from the preceding particles. In terms of viscosity, it remains constant regardless of the rate of shear applied to the fluid in the cavity realm and precisely represents Newtonian behavior. This is in accordance with our remark following Eq. (21).

4.2. Two Newtonian extremes

As mentioned in Section 2, extreme values of β in the expression (21) will correspond to different Newtonian rheologies. To capture these scenarios using the numerical approach ((26), (28)) we cannot use the expression (21) for μ in (26), as we would need to compute divisions by very small numbers for both large and small values of β. Therefore, we adopt the Kapur and Gupta [9] approach, where the quantities in Eq. (32) below be denoted by η_0 and η_∞. However, for analysis purposes, both these quantities are represented by η. Thus, for very small reference τ_0, and using a Taylor expansion around $\frac{\tau^2}{2\tau_0^2}$ and neglecting higher-order terms, μ can be approximated by $\mu(\tau^2) \approx 1 + \frac{2(\lambda-1)\tau_0^2}{\tau^2}$. Similarly, for large reference stresses, the approximation $\mu(\tau^2) \approx 1 + \frac{(\lambda-1)\tau^2}{2\tau_0^2}$ can be obtained. Therefore, for the simulations corresponding to $\beta \to 0$ and $\beta \to \infty$ we consider, in (26), μ given by

$$\mu(\tau^2) = \eta = \begin{cases} 1 + \frac{2(\lambda-1)\beta^2}{\tau^2} & \text{if } \beta \ll 1, \\ 1 + \frac{(\lambda-1)\tau^2}{2\beta^2} & \text{if } \beta \gg 1 \end{cases} \tag{32}$$

In Fig. 9, we represent the viscosity for the results obtained for $\beta = 1e^{-3}$ to represent the case when $\beta \to 0$ (top row), and for $\beta = 1e^{6}$ to represent the case when $\beta \to \infty$ (bottom row). On the first column we can see the shear-thickening solution while the shear-thinning is represented on the second column. As we can see, the viscosity is nearly constant for all the cases.

Thus this model provides a thorough explanation of the fluid's response across all reference shear stress regimes, emphasizing the transition from Newtonian to non-Newtonian between the two extremes (the first four rows of Fig. 8) and then back to Newtonian like case at the two extremes (Fig. 9).

4.3. Coupled thermal analysis

Now, we address the fully coupled model, Eqs. (26)–(29), in order to investigate the influence of the relevant parameters. At first, we observed the velocity profiles and the isotherms at various time intervals. We aimed to investigate the impact of shear-thickening and thinning on thermal behavior and fluid flow. As we will see, significant changes along the time interval [0,3] can be observed, until a steady state is achieved. The latter can be appreciated for the representations corresponding to $t = 3$. In Fig. 10, we illustrate how the flow dynamics and heat transfer characteristics associated with shear-thickening and shear-thinning are distinctly revealed by the influence of suction along the top and bottom walls of the cavity.

Although not immediately apparent, a closer observation reveals distinct variations in both the velocity and temperature fields. In order to appreciate such differences, we have quantified these in the third column. As it can be observed, the differences are quite significant for initial times ($t = 0.5$) and become less prominent when reaching the steady-state ($t = 3$). We observed that for the suction scenario, the fluid flows toward the right wall of the cavity as a whole and the heat diffusion near the heated wall is more pronounced. We also observed that in the lower part of the cavity, fluid particles initially rise due to heat flux and then slightly descend toward the right open-end.

In Fig. 11, we depict the same type of results for the blowing scenario. Again we observe some differences between shear-thickening and shear-thinning cases. In terms of viscosity, these differences become less prominent when time advances. We observe that the fluid tends to flow toward the left wall of the cavity and that the heat distribution near the heated wall (left wall) is less pronounced than in the case of suction. We also observed that in the upper part of the cavity, fluid particles initially rise due to heat flux at the wall and then slightly less descend toward the right open-end. In the subsequent figures, we give a single parametric analysis for the sake of simplicity and clarity in the discussion. We specifically vary the parameters Gr and Re for suction and blowing scenarios while keeping λ, β, and Pr fixed.

In Fig. 12, we illustrate the impact of Gr on velocity, viscosity, and isotherms in the presence of suction ($s = 1$). The Grashof number

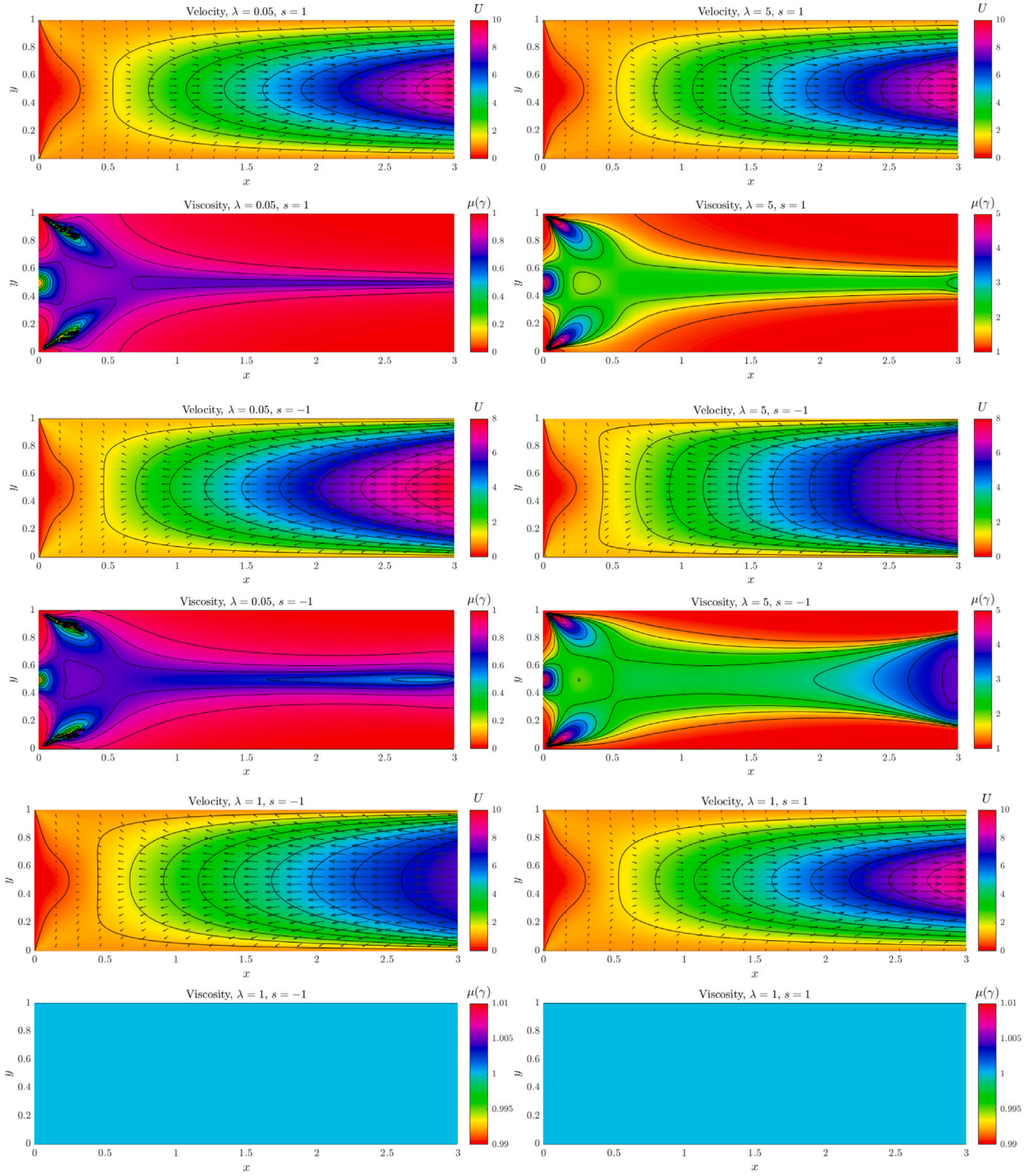

Fig. 8. Combined velocity field, velocity vectors, and viscosity profiles for varying λ and s, with fixed $\beta = 2$, $Re = 10$, and $t = 3$.

measures the relative strength of buoyancy forces compared to viscous forces in a fluid. As Gr increases, buoyancy forces become more dominant over viscous forces, intensifying natural convection currents. Consequently, the velocity of the fluid increases with higher Gr, driven by larger temperature differences or reduced viscosity, which enhance buoyancy-driven flow. From Fig. 12 (first row), it is evident that as Gr increases, the fluid velocity within the cavity rises significantly. The second row of Fig. 12 highlights the effects of viscosity, which are influenced by the interaction between shear rates and flow dynamics. These effects become more prominent in regions where buoyancy-driven flow is stronger. Additionally, the temperature difference created by the heated wall of the cavity generates pronounced upward motion of the fluid, as observed in the isotherms (third row). The enhanced buoyancy forces further strengthen convection currents, facilitating the upward transport of fluid particles and reinforcing the overall flow dynamics shown in the first and third rows of Fig. 12.

Similarly, when blowing ($s = -1$) occurs alongside increasing Gr, as shown in Fig. 13, the combined influence of dominant buoyancy forces and fluid blowing leads to more pronounced flow behavior near the cavity's upper horizontal wall. The velocity in these regions increases significantly due to the upward momentum generated by the synergistic effects of buoyancy and blowing. Additionally, as depicted in Fig.

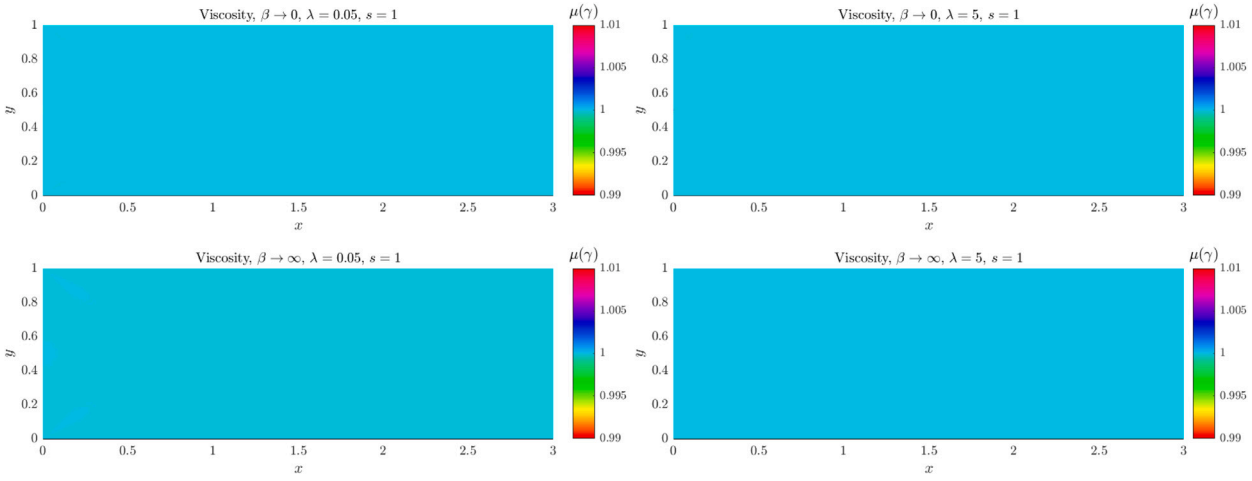

Fig. 9. A nearly Newtonian behavior at the two extremes.

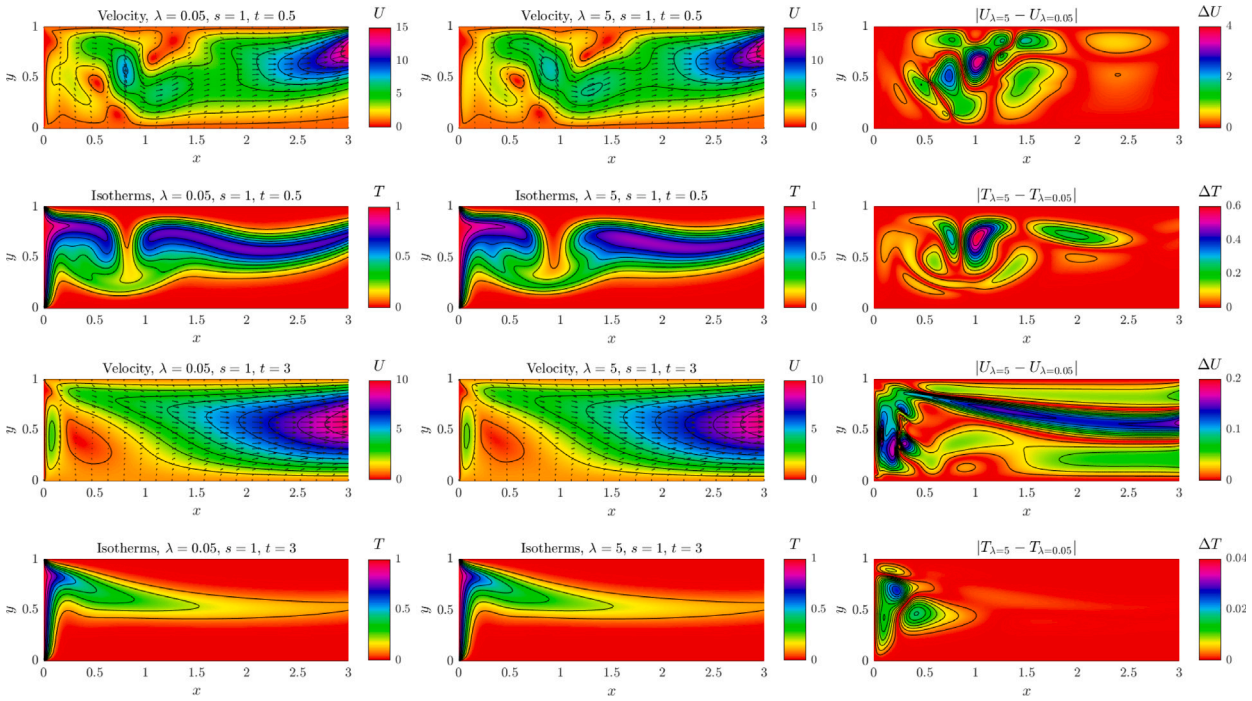

Fig. 10. Combined velocity field, velocity vectors, and isotherms at several time steps for varying λ, with fixed $\beta = 2$, $Pr = 7$ and $Re = 10$.

13 (first and second rows), the viscosity increases in response to the intensified shear forces caused by the stronger flow dynamics.

When the fundamental parameter Re increases under strong suction, inertial forces become more dominant, indicating that the flow is increasingly influenced by the convective transport of momentum. This yields to a significant increase in velocity magnitude within the cavity, as shown in Fig. 14 (first row). The increase in fluid inertia causes the fluid particles to move faster, enhancing the overall velocity. Additionally, the rise in shear rate leads to a more symmetric viscosity distribution across the cavity, as viscous forces diminish in regions with strong velocity gradients. This behavior is depicted in Fig. 14 (second row). As Re increases, the convective terms in the energy equation also become more dominant than the diffusive terms, intensifying the convection effect. Consequently, the isotherms become more concentrated along the cavity's centre line ($y = 0.5$), as shown in Fig. 14 (third row). This phenomenon is attributed to the higher fluid velocity, which effectively transports heat towards the centre of the domain.

In contrast, blowing ($s = -1$) significantly alters the flow structure. At higher Re, the increased fluid inertia causes the bulk flow to resist changes, complicating recirculation patterns and slowing down the flow in certain regions, as illustrated in Fig. 15. Furthermore, the velocity gradients near the walls result in lower shear rates in specific areas, leading to higher effective viscosity. This occurs because the fluid exhibits reduced resistance to deformation at lower shear rates, as depicted in Fig. 15 (second row). Moreover, at higher Re, the isotherms spread more unevenly under blowing, resulting in a less distinct thermal gradient compared to the suction case. This effect is evident in Fig. 15 (third row), where the distribution of heat becomes more irregular due to the altered flow dynamics.

4.4. Local and average nusselt numbers

Based on industry observations, we define the local Nusselt number Nu as an important metric for understanding heat transfer dynamics.

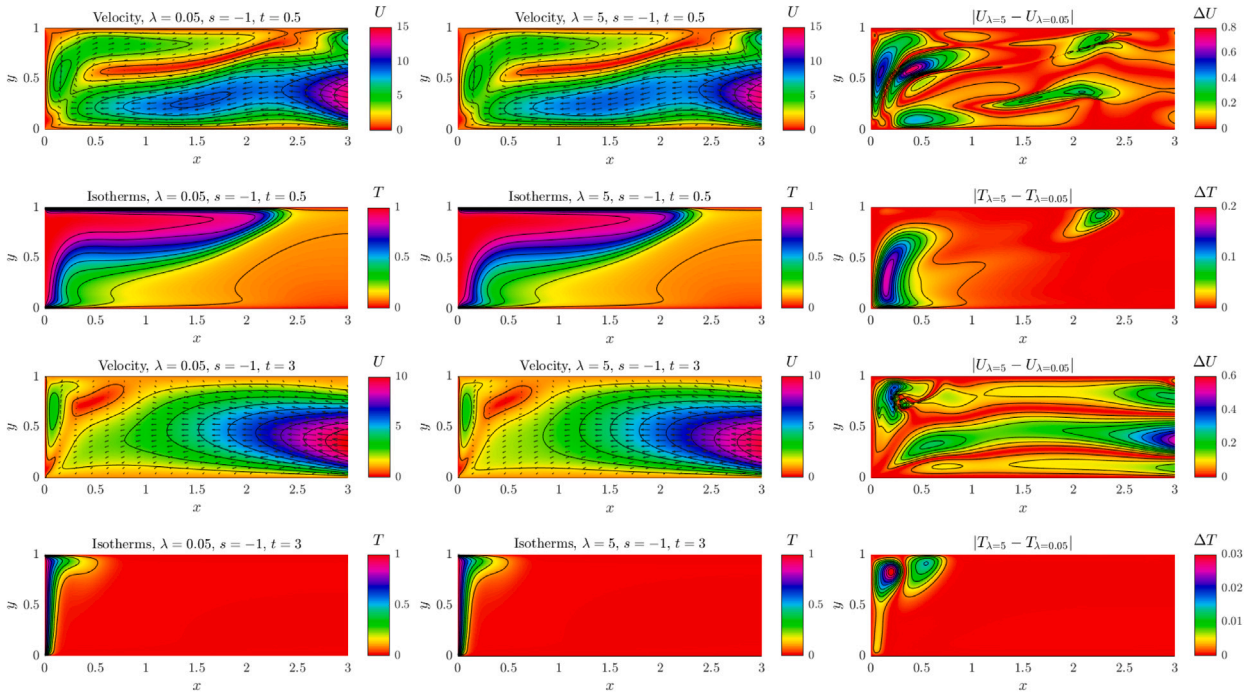

Fig. 11. Combined velocity field, velocity vectors, and isotherms at several time steps for varying λ, with fixed $\beta = 2$, $Pr = 7$ and $Re = 10$.

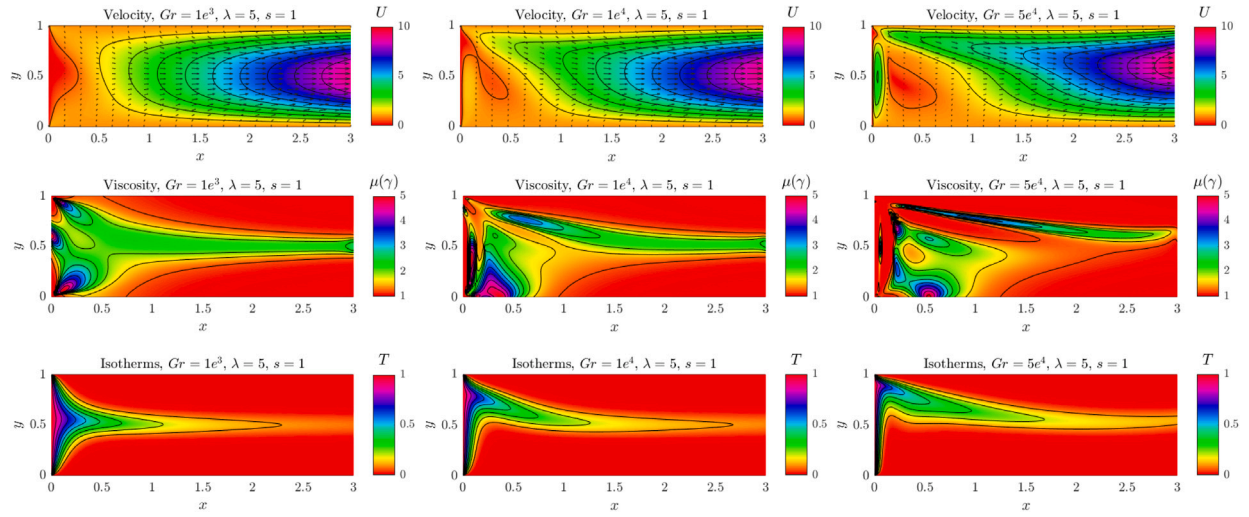

Fig. 12. Combined velocity field, velocity vectors, viscosity and isotherms for varying Gr, with fixed $\beta = 2$, $Pr = 7$, $Re = 10$, and $t = 3$.

This dimensionless heat transfer rate from the left vertical heated wall [29], can be stated mathematically as follows:

$$Nu = -\frac{\partial T}{\partial x}\Big|_{x=0}, \tag{33}$$

while the average Nusselt number Nu_{avg} is calculated using the formula:

$$Nu_{avg} = \int_0^1 Nu\, dy \qquad \text{at} \quad x = 0. \tag{34}$$

Now we discuss the impact of the involved parameters on these metrics. Fig. 16 (top row) illustrates the impact of Gr on the local Nusselt number at the heated wall, particularly in cases involving fluid blowing or suction via the permeable surface. The graphical result demonstrates that an elevation in Gr is associated with an enhanced intensity of local heat transfer. Furthermore, the heat transmission from the left vertical surface exhibits a declining tendency at the bottom and an ascending trend toward the top. Comparing the situations of $s = 1$ (suction) and $s = -1$ (blowing), it is clear that the heat transfer rate is significantly higher during the blowing than during suction. This disparity improves as the value of Gr increases. Fig. 16 (bottom row) also illustrates the average Nusselt number for various reference shear stresses. As already depicted in Fig. 9, at both low and hight shear stresses, nearly Newtonian behavior is observed at the two Newtonian

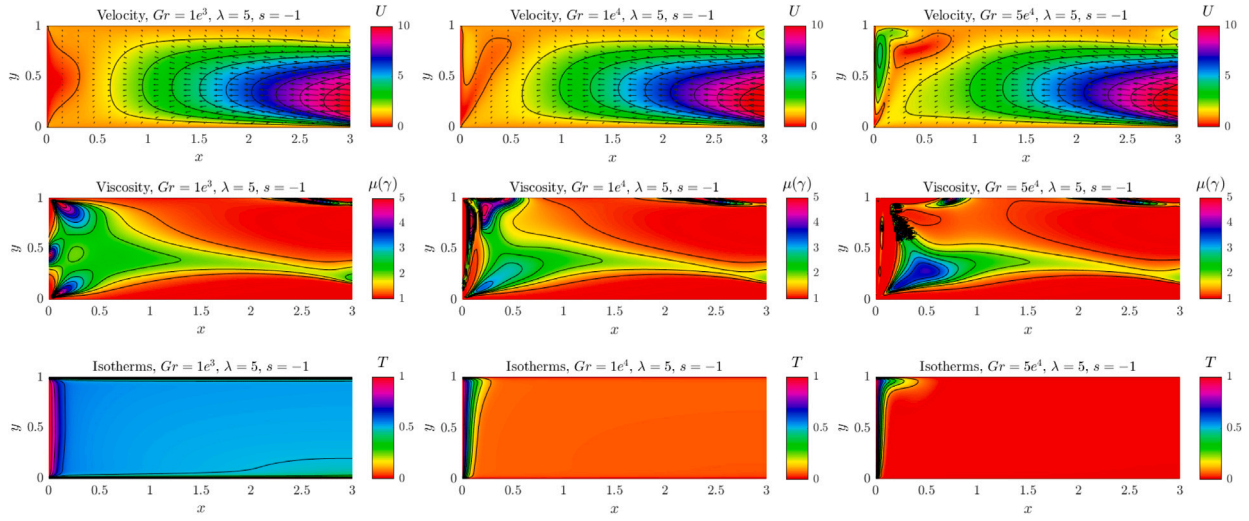

Fig. 13. Combined velocity field, velocity vectors, viscosity and isotherms for varying Gr, with fixed $\beta = 2$, $Pr = 7$, $Re = 10$, and $t = 3$.

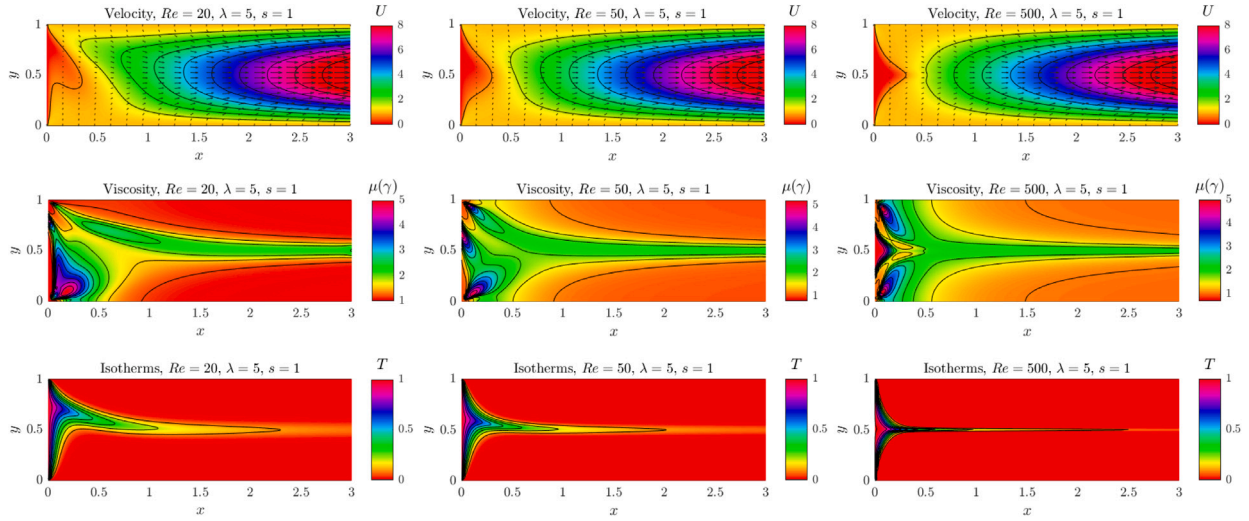

Fig. 14. Combined velocity field, velocity vectors, viscosity and isotherms for varying Re, with fixed $\beta = 2$, $Pr = 7$, $Gr = 1e^4$, and $t = 3$.

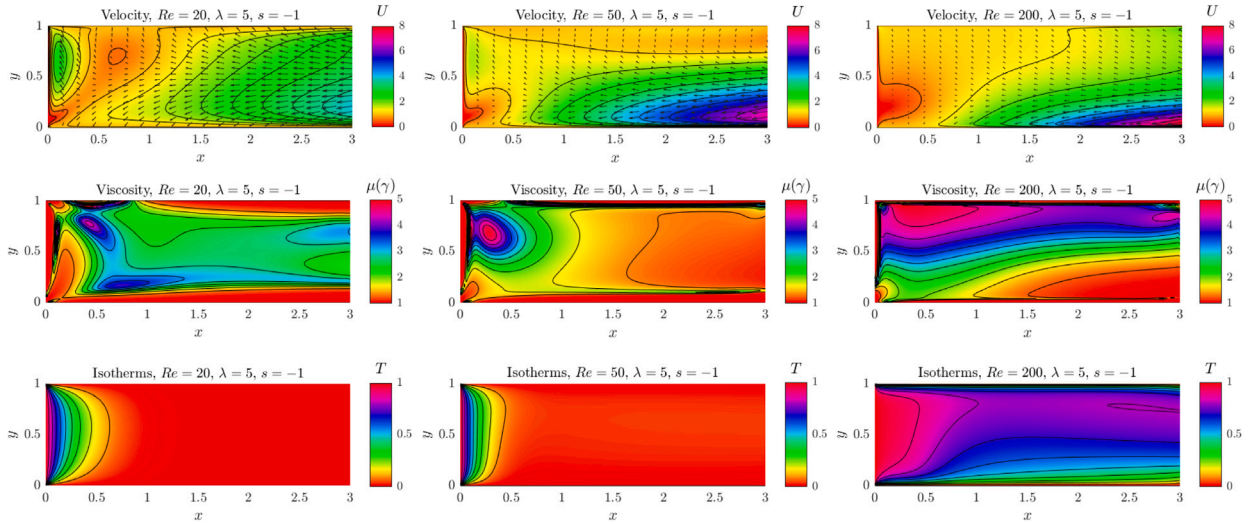

Fig. 15. Combined velocity field, velocity vectors, viscosity and isotherms for varying Re, with fixed $\beta = 2$, $Pr = 7$, $Gr = 1e^4$, and $t = 3$.

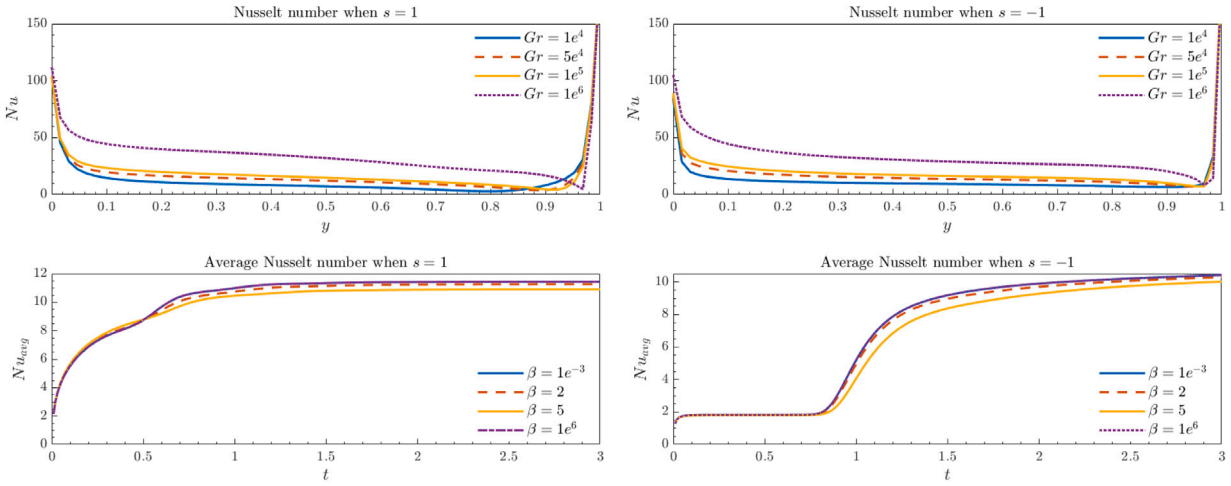

Fig. 16. Numerical values of local and average Nusselt numbers at the heated surface for varying Gr and β, considering the effects of suction ($s = 1$), blowing ($s = -1$), with fixed $\lambda = 5$, $Re = 10$, $Pr = 7$, and $t = 3$.

extremes, as indicated by the limits of $\beta \to 0$ and $\beta \to \infty$, respectively. Nonetheless, we see an increasing trend in the average Nusselt number for $\lambda = 5$ and $s = 1$ over the range of shear stress values indicating the intermediate of non-Newtonian behavior. In a similar manner, when $s = -1$, Fig. 16 again show Newtonian behavior at both the low and high reference shear stresses. This case exhibits an increasing average Nusselt number across the spectrum of shear stress values that represent non-Newtonian behavior. The average Nusselt number increases with the Grashof number for all cases, as evidenced by the results in Tables 4 and 5. Given the ratio comparisons in Tables 4 and 5, for instance, the average Nusselt number is 1.247 times higher than the base value ($Gr = 1e^4$) when $Gr = 5e^4$ and 1.406 times higher than the base value when $Gr = 1e^5$ for $s = 1$ and $\lambda = 5$. The tabulated data also confirms that enhanced buoyancy facilitates convective heat transfer. Compared to $s = 1$, the configuration with $s = -1$ demonstrates a larger relative enhancement and a higher average Nusselt number for both values of the RPP parameter λ. This suggests that blowing facilitates efficient heat transport and stronger circulation. The results highlight that the enhancement of heat transfer in the flow system is collectively affected by buoyancy intensity, wall movement, and the non-Newtonian rheological parameter λ.

Table 4
Comparison of average Nusselt number for $s = \pm 1$ and $\lambda = 5$ at various Grashof numbers, with fixed $Re = 10$, $\beta = 2$, $Pr = 7$, and $t = 3$. Percent increase and relative ratio are calculated with respect to the baseline case $Gr = 1 \times 10^4$.

Gr	$s = 1$, $\lambda = 5$			$s = -1$, $\lambda = 5$		
	Nu_{avg}	Increase (%)	Ratio	Nu_{avg}	Increase (%)	Ratio
1×10^4	14.2575	0.00	1.000	12.9761	0.00	1.000
5×10^4	17.7726	24.65	1.247	17.9795	38.56	1.3856
1×10^5	20.0490	40.62	1.406	20.6752	59.33	1.593

Table 5
Comparison of average Nusselt number for $s = \pm 1$ and $\lambda = 0.05$ at various Grashof numbers, with fixed $Re = 10$, $\beta = 2$, $Pr = 7$, and $t = 3$. Percent increase and relative ratio are calculated with respect to the baseline case $Gr = 1 \times 10^4$.

Gr	$s = 1$, $\lambda = 0.05$			$s = -1$, $\lambda = 0.05$		
	Nu_{avg}	Increase (%)	Ratio	Nu_{avg}	Increase (%)	Ratio
1×10^4	14.4503	0.00	1.000	13.0963	0.00	1.000
5×10^4	17.8481	23.51	1.235	18.0433	37.77	1.378
1×10^5	20.1019	39.11	1.391	20.7201	58.21	1.582

5. Concluding remarks

This study used a semi-implicit scheme in conjunction with finite element method to look in detail at the unsteady buoyancy-driven flow and heat transfer of a non-Newtonian RPP fluid in an open-ended cavity. Our study was mainly about figuring out how shear-thickening and shear-thinning affect the movement and temperature of fluids under a variety of flow conditions, such as when they are suctioned or blown and when Grashof and Reynolds numbers change. The results show that non-Newtonian RPP fluid behaves very differently under the influence of various flow conditions compared to Newtonian fluid, especially when it comes to changes in shear rate and buoyancy forces. The main findings of the present investigation are as follows:

- In the presence of suction and absence of temperature variable, the increase in viscosity due to shear-thickening was more pronounced near the walls of the cavity because of velocity gradient, causing the fluid to resist flow more in these regions compared to the center of the cavity. It was also observed that the viscosity of the fluid is minimum where the velocity gradient is steeper due to the shear-thinning nature of the fluid.
- Following the same pattern for blowing scenario, we also observed that for the case of shear-thickening, again the increased viscosity was comparatively more pronounced near the upper and bottom walls of the cavity than at the center of the cavity. Also, the velocity magnitude tends to be higher near the walls, when compared to the suction case, especially closer to the open-end wall. On the other hand, it was also observed that the viscosity is lower where the velocity gradient is steeper due to the shear-thinning nature of the fluid.
- The model also provides a thorough explanation of the fluid's response across all reference shear stress regimes, emphasizing the transition from Newtonian to non-Newtonian between and at the two extremes.
- We observed the impact of a higher Grashof number on velocity profiles, viscosity distributions, and temperature profiles. The magnitude of the fluid velocity increased due to higher Grashof number. As to the viscosity, the interaction between shear rates and flow dynamics became more prominent in regions where

buoyancy-driven flow was stronger. Additionally, the temperature difference created due to the heated wall generated a pronounced upward motion of the fluid that further strengthened convection currents, facilitated the upward transport of fluid particles, and reinforced the overall flow dynamics. Meanwhile, as Reynolds number increased, the impact of convection became more pronounced. This led to more uniform velocity distributions and more concentrated isotherms resulting in a less distinct thermal gradient compared to the suction case. This observation highlighted the dominance of inertial forces over viscous forces with high Reynolds numbers.

- Local Nusselt numbers analysis show that blowing fluid through the permeable surface results in a higher heat transfer rate than suction. Furthermore, the average Nusselt number increases as the Grashof number increases, indicating that convective transport is facilitated by stronger buoyancy effects. At $Gr = 1e^4$, the configuration with $s = 1$ yields a higher Nu_{avg} than $s = -1$. However, when Gr increases, this trend reverses. For both $\lambda = 5$ and $\lambda = 0.05$, increasing the Grashof number yields an even clearer distinction between the two scenarios: while the $s = 1$ case shows increase of 23–41%, the $s = -1$ case exhibits larger enhancements of 38–59% showing that at higher buoyancy forces, blowing contributes in stabilizing and strengthening the buoyancy-induced circulation, thus enhancing the heat transfer rate. These findings are consistent with both the graphical and tabular data.

This work offered critical insights into the influence of non-Newtonian features on fluid dynamics and heat transfer within an open-end cavity, highlighting their importance in engineering and industrial applications. The results provide a basis for additional investigation into the optimization of processes using non-Newtonian fluids. In the future research, we plan to broaden the existing analysis to include more complex three-dimensional configurations and perform a comparative study of free, forced, and mixed convection regimes. Additionally, in order to make the proposed model more applicable to biological flow systems and engineering applications, we intend to investigate the effects of mixed convection on nanofluids.

CRediT authorship contribution statement

Razi Khan: Writing – original draft, Visualization, Validation, Software, Investigation, Funding acquisition, Formal analysis, Conceptualization. **Jorge Tiago:** Writing – review & editing, Supervision, Software, Resources, Project administration, Methodology, Funding acquisition, Conceptualization. **Adeel Ahmad:** Writing – review & editing, Supervision, Investigation, Formal analysis, Conceptualization. **Paolo Valdiserri:** Writing – review & editing, Resources, Methodology, Formal analysis. **Eugenia Rossi di Schio:** Writing – review & editing, Visualization, Validation, Resources, Formal analysis.

Declaration of competing interest

The authors declare that they have no known competing financial interests or personal relationships that could have appeared to influence the work reported in this paper.

Acknowledgments

This work was supported by FCT – Fundacao para a Ciencia e Tecnologia through the research project PTDC/MAT-APL/7076/2020, https://doi.org/10.54499/PTDC/MAT-APL/7076/2020 and CEMAT's research project UIDB/04621/2020/IST-ID.

Nomenclature:

Symbol	Dimension/Unit	Meaning
$\overset{*}{u}, \overset{*}{v}$	m s^{-1}	Velocity in $\overset{*}{x}$ and $\overset{*}{y}$ directions
$\overset{*}{x}, \overset{*}{y}$	m	Cartesian coordinates
$\overset{*}{t}$	s	Time
$\overset{*}{T}$	°C	Temperature
$\overset{*}{C}$	kg m^{-1} s^{-2}	Cauchy stress tensor
$\overset{*}{\tau}$	kg m^{-1} s^{-2}	Deviatoric stress tensor
$\overset{*}{\tau_0}$	kg m^{-1} s^{-2}	Reference shear stress tensor
μ_∞	kg m^{-1} s^{-1}	Upper Newtonian limiting viscosity
μ_0	kg m^{-1} s^{-1}	Zero-shear/ lower Newtonian limiting viscosity
ρ	kg m^{-3}	Density
$\boldsymbol{g}$	m s^{-2}	Gravitational acceleration vector
β_T	K^{-1}	Thermal expansion coefficient
$\overset{*}{p}$	kg m^{-1} s^{-2}	Pressure
$\overset{*}{e}$	s^{-1}	Strain-rate
α	m^2 s^{-1}	Thermal diffusivity
V_0	m s^{-1}	Transpiration Velocity
L	m	Width of the cavity
H	m	Height of the cavity
u, v	–	Dimensionless Velocity components
x, y	–	Dimensionless Cartesian coordinates
t	–	Dimensionless time
T	–	Dimensionless temperature
$\mathbf{C}$	–	Dimensionless Cauchy stress tensor
τ	–	Dimensionless deviatoric tensor
A	–	Length of the cavity
s	–	Suction/ blowing parameter
λ	–	Reiner–Philippoff fluid parameter
$\beta = \sqrt{\tau_0^2}$	–	Dimensionless reference stress tensor
Gr	–	Grashof number
Re	–	Reynolds number
Pr	–	Prandtl number
Ra	–	Rayleigh number
ψ	–	Dimensionless stream function
Nu	–	Local Nusselt number
Nu_{avg}	–	Average Nusselt number

Data availability

Data will be made available on request.

References

[1] G.R. Kefayati, H. Tang, Three-dimensional lattice Boltzmann simulation on thermosolutal convection and entropy generation of Carreau-Yasuda fluids, Int. J. Heat Mass Transfer 131 (2019) 346–364, http://dx.doi.org/10.1016/j.ijheatmasstransfer.2018.11.076.

[2] M.S. Khan, S. Ahmad, Z. Shah, A. Alshehri, N. Vrinceanu, H.A. Garalleh, Computational study of double diffusive MHD natural convection flow of non-Newtonian fluid between concentric cylinders, Results Eng. 21 (2024) 101925, http://dx.doi.org/10.1016/j.rineng.2024.101925.

[3] L. Fusi, A. Farina, G. Saccomandi, K. Rajagopal, Lubrication approximation of flows of a special class of non-Newtonian fluids defined by rate type constitutive equations, Appl. Math. Model. 60 (2018) 508–525, http://dx.doi.org/10.1016/j.apm.2018.03.038.

[4] P.P. Roy, S. Chowdhury, M.H. Raj, M.Q. Islam, S. Saha, Forced, natural and mixed convection of Non-Newtonian fluid flows in a square chamber with moving lid and discrete bottom heating, Results Eng. 17 (2023) 100939, http://dx.doi.org/10.1016/j.rineng.2023.100939.

[5] T.-Y. Na, Boundary layer flow of Reiner-Philippoff fluids, Int. J. Non-Linear Mech. 29 (6) (1994) 871–877, http://dx.doi.org/10.1016/0020-7462(94)90059-0.

[6] A. Hansen, T. Na, Similarity solutions of laminar, incompressible boundary layer equations of non-Newtonian fluids, 1968, http://dx.doi.org/10.1115/1.3605067.

[7] T. Sajid, S. Tanveer, M. Munsab, Z. Sabir, Impact of oxytactic microorganisms and variable species diffusivity on blood-gold Reiner–Philippoff nanofluid, Appl. Nanosci. 11 (1) (2021) 321–333, http://dx.doi.org/10.1007/s13204-020-01581-x.

[8] J. Iqbal, F. Abbasi, I. Ali, Heat transfer analysis for magnetohydrodynamic peristalsis of Reiner–Philippoff fluid: Application of an artificial neural network, Phys. Fluids 36 (4) (2024) http://dx.doi.org/10.1063/5.0207600.

[9] J. Kapur, R. Gupta, Two dimensional flow of Reiner-Philippoff fluids in the inlet length of a straight channel, Appl. Sci. Res. Sect. A 14 (1965) 13–24, http://dx.doi.org/10.1007/BF00382227.

[10] S. Ghoshal, Dispersion of solutes in non-Newtonian flows through a circular tube, Chem. Eng. Sci. 26 (2) (1971) 185–188, http://dx.doi.org/10.1016/0009-2509(71)80002-7.

[11] K. Yam, S. Harris, D. Ingham, I. Pop, Boundary-layer flow of Reiner–Philippoff fluids past a stretching wedge, Int. J. Non-Linear Mech. 44 (10) (2009) 1056–1062, http://dx.doi.org/10.1016/j.ijnonlinmec.2009.08.006.

[12] M. Gnaneswara Reddy, M. Sudharani, K. Ganesh Kumar, A.J. Chamkha, G. Lorenzini, Physical aspects of Darcy–Forchheimer flow and dissipative heat transfer of Reiner–Philippoff fluid, J. Therm. Anal. Calorim. 141 (2020) 829–838, http://dx.doi.org/10.1007/s10973-019-09072-0.

[13] A. Ishaq, E.A. Algehyne, A. Ahmad, F. Mallawi, Magneto-hydrodynamic flow of Reiner-Philippoff fluid: Stability analysis, Phys. Scr. 96 (3) (2020) 035203, http://dx.doi.org/10.1088/1402-4896/abd360.

[14] K.G. Kumar, M.G. Reddy, M.I. Khan, F. Alzahrani, M.I. Khan, E.R. El-Zahar, Heat transfer and melting flow ofa reiner-philippoff fluid over a surface with Darcy-forchheimer medium, Case Stud. Therm. Eng. 28 (2021) 101649, http://dx.doi.org/10.1016/j.csite.2021.101649.

[15] M. Kumar, P.K. Mondal, Radiative and hydromagnetic heat transfer analysis of a Reiner–Philippoff fluid, J. Thermophys. Heat Transfer 37 (1) (2023) 213–226, http://dx.doi.org/10.2514/1.T6625.

[16] M.B. Arain, A. Idris, S. Shaheen, T. Muhammad, J. Hu, Theoretical analysis of Reiner-Philippoff fluid flow in two layers due to metachronal propulsion: Subject to surrounding temperature, Case Stud. Therm. Eng. 53 (2024) 103789, http://dx.doi.org/10.1016/j.csite.2023.103789.

[17] M. Tahir, A. Ahmad, Impact of pseudoplaticity and dilatancy of fluid on peristaltic flow and heat transfer: Reiner-philippoff fluid model, Adv. Mech. Eng. 12 (12) (2020) 1687814020981184, http://dx.doi.org/10.1177/1687814020981184.

[18] I. Waini, N.S. Khashi'ie, A.R.M. Kasim, N.A. Zainal, A. Ishak, I. Pop, Radiative heat transfer of Reiner–Philippoff fluid flow past a nonlinearly shrinking sheet: Dual solutions and stability analysis, Chinese J. Phys. 77 (2022) 45–56, http://dx.doi.org/10.1016/j.cjph.2021.11.037.

[19] P.-Y. Xiong, Y.-M. Chu, M.I. Khan, S.A. Khan, S. Abbas, Entropy optimized Darcy-Forchheimer flow of Reiner-Philippoff fluid with chemical reaction, Comput. Theor. Chem. 1200 (2021) 113222, http://dx.doi.org/10.1016/j.comptc.2021.113222.

[20] Y.O. Tijani, S.D. Oloniiju, M.O. Oni, M.T. Akolade, Surface dynamics and thermophysical mechanics on Reiner–Philippoff fluid flow, Internat. J. Modern Phys. B (2023) 2450339, http://dx.doi.org/10.1142/S0217979224503399.

[21] L. Carreto-Hernandez, S. Moya, C. Varela-Boydo, I.J. Sosa, W. Báez-García, V. Reyes, J. Morales, Analysis of natural convection in a representative cavity of a room considering oscillatory boundary conditions: An experimental and numerical approach, Int. J. Therm. Sci. 206 (2024) 109357, http://dx.doi.org/10.1016/j.ijthermalsci.2024.109357.

[22] H. Skok, S. Ramadhyani, R. Schoenhals, Natural convection in a side-facing open cavity, Int. J. Heat Fluid Flow 12 (1) (1991) 36–45, http://dx.doi.org/10.1016/0142-727X(91)90006-H.

[23] O. Aydm, Aiding and opposing mechanisms of mixed convection in a shear- and buoyancy-driven cavity, Int. Commun. Heat Mass Transfer 26 (7) (1999) 1019–1028, http://dx.doi.org/10.1016/S0735-1933(99)00091-3.

[24] K. Khanafer, K. Vafai, Buoyancy-driven flow and heat transfer in open-ended enclosures: elimination of the extended boundaries, Int. J. Heat Mass Transfer 43 (22) (2000) 4087–4100, http://dx.doi.org/10.1016/S0017-9310(00)00047-8.

[25] D. Angirasa, M. Pourquie, F. Nieuwstadt, Numerical study of transient and steady laminar buoyancy-driven flows and heat transfer in a square open cavity, Numer. Heat Transfer 22 (2) (1992) 223–239, http://dx.doi.org/10.1080/10407789208944766.

[26] D.L. Stefanovic, H.G. Stefan, Simulation of transient cavity flows driven by buoyancy and shear, J. Hydraul. Res. 38 (3) (2000) 181–195, http://dx.doi.org/10.1080/00221680009498336.

[27] O. Polat, E. Bilgen, Laminar natural convection in inclined open shallow cavities, Int. J. Therm. Sci. 41 (4) (2002) 360–368, http://dx.doi.org/10.1016/S1290-0729(02)01326-1.

[28] E. Bilgen, Natural convection in cavities with a thin fin on the hot wall, Int. J. Heat Mass Transfer 48 (17) (2005) 3493–3505, http://dx.doi.org/10.1016/j.ijheatmasstransfer.2005.03.016.

[29] M. Hossain, S. Asghar, R. Subba Reddy Gorla, Buoyancy-driven flow of a viscous incompressible fluid in an open-ended rectangular cavity with permeable horizontal surfaces, Internat. J. Numer. Methods Heat Fluid Flow 20 (7) (2010) 759–772, http://dx.doi.org/10.1108/09615531011065557.

[30] A. Lefauve, P. Linden, Buoyancy-driven exchange flows in inclined ducts, J. Fluid Mech. 893 (2020) A2, http://dx.doi.org/10.1017/jfm.2020.212.

[31] E. Chen, F. Xu, Transient thermocapillary convection flows in a rectangular cavity with an evenly heated lateral wall, Phys. Fluids 33 (1) (2021) http://dx.doi.org/10.1063/5.0034650.

[32] M. Shahabadi, S. Mehryan, M. Ghalambaz, M. Ismael, Controlling the natural convection of a non-Newtonian fluid using a flexible fin, Appl. Math. Model. 92 (2021) 669–686, http://dx.doi.org/10.1016/j.apm.2020.11.029.

[33] B. Joshi, A. Sengupta, P. Sundaram, Exploring role of aspect ratio for compressible flow in a rectangular lid-driven cavity with a vertical temperature gradient, Phys. Fluids 35 (6) (2023) http://dx.doi.org/10.1063/5.01558510.

[34] D.T. Yaseen, M.A. Ismael, Analysis of power law fluid-structure interaction in an open trapezoidal cavity, Int. J. Mech. Sci. 174 (2020) 105481, http://dx.doi.org/10.1016/j.ijmecsci.2020.105481.

[35] K. Chandra, S. Sabet, H. Kaya, B. Buonomo, O. Manca, A transient numerical approach for phase change material effect on mixed convection in an open cavity, Int. Commun. Heat Mass Transfer 148 (2023) 107051, http://dx.doi.org/10.1016/j.icheatmasstransfer.2023.107051.

[36] T. Xu, J.-I. Choi, Numerical investigation of flow and heat transfer characteristics in buoyancy-driven convection around cylinder arrays within an enclosure, Phys. Fluids 37 (2) (2025) http://dx.doi.org/10.1063/5.0251568.

[37] A.I. Alsabery, M.A. Ismael, S.K. Al-Hadraawy, M. Ghalambaz, I. Hashim, A.J. Chamkha, Fluid-structure interaction model of blood flow in abdominal aortic aneurysms with thermic treatment, Alex. Eng. J. 64 (2023) 81–95, http://dx.doi.org/10.1016/j.aej.2022.08.032.

[38] A. Tulu, M. Hirpho, M. Sohail, Modeling and simulation of mixed convection flow with viscous dissipation in a lid-driven hexagonal cavity using finite element method, Int. J. Thermofluids 22 (2024) 100702, http://dx.doi.org/10.1016/j.ijft.2024.100702.

[39] Q. Lu, R. Pal, Steady shear rheology and surface activity of polymer-surfactant mixtures, Polymers 17 (3) (2025) 364, http://dx.doi.org/10.3390/polym17030364.

[40] Y. Rabin, H.C. Öttinger, Dilute polymer solutions: Internal viscosity, dynamic scaling, shear thinning and frequency-dependent viscosity, Europhys. Lett. 13 (5) (1990) 423, http://dx.doi.org/10.1209/0295-5075/13/5/008.

[41] E. Brown, H.M. Jaeger, Shear thickening in concentrated suspensions: phenomenology, mechanisms and relations to jamming, Rep. Progr. Phys. 77 (4) (2014) 046602, http://dx.doi.org/10.1088/0034-4885/77/4/046602.

[42] A. Quarteroni, A. Valli, Numerical Approximation of Partial Differential Equations, vol. 23, Springer Science & Business Media, 2008, http://dx.doi.org/10.1007/978-3-540-85268-1.

[43] A. Quarteroni, L. Formaggia, Mathematical modelling and numerical simulation of the cardiovascular system, Handb. Numer. Anal. 12 (2004) 3–127.

[44] F. Hecht, New development in FreeFem++, J. Numer. Math. 20 (3–4) (2012) 251–265, http://dx.doi.org/10.1515/jnum-2012-0013, 3043640.

[45] U. Ghia, K.N. Ghia, C. Shin, High-Re solutions for incompressible flow using the Navier-Stokes equations and a multigrid method, J. Comput. Phys. 48 (3) (1982) 387–411, http://dx.doi.org/10.1016/0021-9991(82)90058-4.

[46] M. Turkyilmazoglu, Driven flow motion by a dually moving lid of a square cavity, Eur. J. Mech. B Fluids 94 (2022) 17–28, http://dx.doi.org/10.1016/j.euromechflu.2022.02.005.

[47] O. Botella, R. Peyret, Benchmark spectral results on the lid-driven cavity flow, Comput. & Fluids 27 (4) (1998) 421–433, http://dx.doi.org/10.1016/S0045-7930(98)00002-4.

[48] A. Malatip, N. Wansophark, P. Dechaumphai, A second-order time-accurate finite element method for analysis of conjugate heat transfer between solid and unsteady viscous flow, J. Mech. Sci. Technol. 23 (2009) 775–789, http://dx.doi.org/10.1007/s12206-008-1115-0.

[49] M. Waheed, Mixed convective heat transfer in rectangular enclosures driven by a continuously moving horizontal plate, Int. J. Heat Mass Transfer 52 (21–22) (2009) 5055–5063, http://dx.doi.org/10.1016/j.ijheatmasstransfer.2009.05.011.

[50] M. Abdelkhalek, Mixed convection in a square cavity by a perturbation technique, Comput. Mater. Sci. 42 (2) (2008) 212–219, http://dx.doi.org/10.1016/j.commatsci.2007.07.004.

[51] K.M. Khanafer, A.J. Chamkha, Mixed convection flow in a lid-driven enclosure filled with a fluid-saturated porous medium, Int. J. Heat Mass Transfer 42 (13) (1999) 2465–2481, http://dx.doi.org/10.1016/S0017-9310(98)00227-0.

[52] R. Iwatsu, J.M. Hyun, K. Kuwahara, Mixed convection in a driven cavity with a stable vertical temperature gradient, Int. J. Heat Mass Transfer 36 (6) (1993) 1601–1608, http://dx.doi.org/10.1016/S0017-9310(05)80069-9.

[53] P. Neofytou, A 3rd order upwind finite volume method for generalised Newtonian fluid flows, Adv. Eng. Softw. 36 (10) (2005) 664–680, http://dx.doi.org/10.1016/j.advengsoft.2005.03.011.

[54] B.C. Bell, K.S. Surana, P-version least squares finite element formulation for two-dimensional, incompressible, non-Newtonian isothermal and non-isothermal fluid flow, Internat. J. Numer. Methods Fluids 18 (2) (1994) 127–162, http://dx.doi.org/10.1002/fld.1650180202.